

# Simulations of rib-roughened rough-to-smooth turbulent channel flows

Umair Ismail<sup>1†</sup>, Tamer A. Zaki<sup>2</sup> and Paul A. Durbin<sup>1</sup>

<sup>1</sup>Department of Aerospace Engineering, Iowa State University, Ames, IA 50011, USA

<sup>2</sup>Department of Mechanical Engineering, Johns Hopkins University, Baltimore, MD 21218, USA

(Received xx; revised xx; accepted xx)

High fidelity simulations of turbulent flow through a channel with a rough wall, followed by a smooth wall, demonstrate a high degree of non-equilibrium within the recovery region. In fact, the recovery of all the flow statistics studied is incomplete by the streamwise exit of the computational domain. Above a thin wall layer, turbulence intensities significantly higher than fully developed, smooth-wall levels persist in the developing region. Within the thin wall layer, the profile shapes for turbulence stresses recover very quickly and wall-normal locations of characteristic peaks are established. However, even in this thin layer, complete recovery of magnitudes of turbulence stresses is exceptionally slow. A similar initially swift but eventually incomplete and slow relaxation behaviour is also shown by the skin friction. Between the turbulence shear and streamwise stresses, the turbulence shear stress shows a comparatively quick rate of recovery above a thin wall layer. Over the developing smooth wall, the balance is not merely between fluxes due to pressure and shear stresses. Strong momentum fluxes, which are directly influenced by the upstream roughness size, contribute significantly to the balance over the developing smooth wall. Curve fits estimate the streamwise distance required by the Reynolds stresses to attain near-fully-developed levels at about  $20\delta - 25\delta$ . An even longer distance, of more than  $50\delta$ , is needed by the mean flow field to approach the fully developed magnitudes. Visualizations and correlations show that large scale eddies that are created above the roughness persist downstream, and sporadically perturb the elongated streaks. These streaks of alternating high and low momentum appear almost instantly after the roughness is removed. The mean flow does not re-establish an equilibrium log layer within the computational domain, and the velocity deficit created by the roughness continues throughout the domain. On the step change in roughness, near the wall, profiles for turbulence kinetic energy dissipation rate,  $\epsilon$ , and energy spectra indicate sharp reduction in energy at small scales. Despite this, reversion towards equilibrium smooth-wall levels is slow, and ultimately incomplete, due to a rather slow adjustment of the turbulence cascade. The non-dimensional roughness height,  $k^+$  ranges from 42 to 254 and the friction velocity Reynolds number at the smooth wall,  $Re_{\tau S}$ , ranges from 284 to 1160 in the various simulations.

## 1. Introduction

It is not uncommon that rough surfaces with significant variation in the roughness height occur in engineering and environmental flows. Examples include gas turbine blades, atmospheric boundary layers, and ship hulls. Idealizations of such non-equilibrium, rough-wall turbulent flows have been investigated by laboratory

† Email address for correspondence: umair@iastate.edu

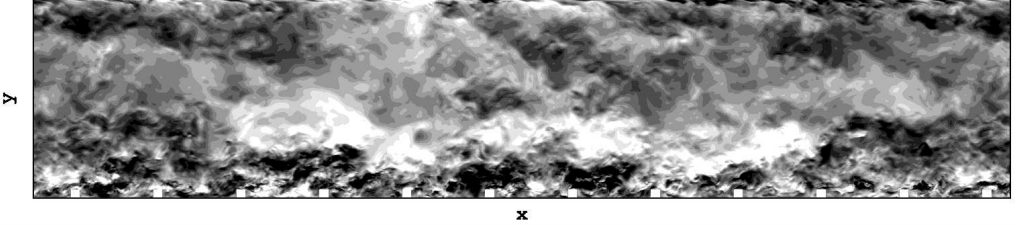


Figure 1: Instantaneous streamwise velocity fluctuations,  $u'$ , in the  $xy$ -plane for a fully developed, rough-wall turbulent channel flow. Scale: white +0.2, black -0.2.

experiments (Antonia & Luxton 1971, 1972; Pearson *et al.* 1997; Cheng & Castro 2002; Jacobi & McKeon 2011). Particularly relevant to the present work, Antonia & Luxton (1972), Hosni & Coleman (1993) and Hanson & Ganapathisubramani (2016) studied the relaxation of fully developed, rough-wall turbulent boundary layers towards fully developed smooth-wall states, on encountering a sudden change in boundary condition, from rough to a smooth (RTS). RTS flows form a subset of more general non-equilibrium rough-wall flows, and are the subject of numerical experiments presented herein. Despite the obvious importance in understanding rough to smooth evolution, to the best of our knowledge, there have been no previous, fully resolved, numerical simulations of RTS flow.

Many high Reynolds, turbulent flows of engineering significance are, in essence, hydrodynamically rough. For such flows the viscous sublayer and buffer layer, that are encountered on smooth walls, are replaced by a roughness sublayer which extends above the surface to between 2 and 5 times the roughness height (Raupach *et al.* 1991). Within this roughness sublayer, in addition to intensification of turbulence, the large-scale structure is enhanced and shows strong interaction with the overlying outer-flow. The high intensity turbulence in this sublayer transfers momentum between the surface and the outer regions — as is clear from the instantaneous streamwise velocity fluctuations,  $u'$ , of a rib-roughened, fully developed turbulent flow in figure 1. Inside the roughness cavities in figure 1, turbulence is characterized by three-dimensional unstable eddies with size of the order of the roughness height (Ikeda & Durbin 2007), which is typical of  $k$ -type rough-wall flows (Perry *et al.* 1969).

In RTS flows, the rough wall structure carries downstream over the smooth wall. The skin friction shows a sharp reduction, as the drag of roughness elements is removed, but followed by a quick recovery towards equilibrium smooth-wall levels. This is accompanied by a comparatively slow recovery of the mean velocity towards the smooth-wall values. This behavior has been seen in RTS lab experiments; in Antonia & Luxton (1972), profiles of both mean velocity and turbulence stresses showed incomplete relaxation by the last measuring station, located at approximately 16 boundary-layer thicknesses downstream of the step change. These authors argued that this slow recovery is a feature of both inner and outer layers. Although they were able to fit conventional log-laws to the mean velocity profiles on the developing smooth wall, the intercept was considerably higher than the fully developed, smooth-wall value of about 5.1. The present simulations show that the log-law is not established, at all, in the recovery region.

More recently, Hanson & Ganapathisubramani (2016), in their RTS boundary layer experiments, with mesh-type and grit-type roughnesses, showed virtually complete recovery of mean velocity profiles, but the streamwise turbulence stresses remained higher than equilibrium all the way to the last measuring station. Hanson & Ganapathisubramani

(2016) proposed the internal boundary height as an appropriate length-scale in the transitional regime. The internal boundary layer height was meant to discriminate between a region influenced by the new boundary condition, and an overlying region, that is primarily determined by the upstream rough-wall. However, except for tracking the outer-peaks of streamwise turbulence stress, and providing a gross demarcation between the two aforementioned regions, the utility of this internal layer concept was rather limited.

The present study aims to contribute to the existing literature on non-equilibrium RTS turbulent flows by (i) being the first, fully resolved computer simulations of transition from a fully developed rough-wall state to the developing smooth-wall behavior in turbulent channel flows, highlighting the non-equilibrium turbulent flow development; (ii) providing an accurate estimation of skin-friction levels, which are difficult to measure by experimental techniques (see [Jacobi & McKeon 2011](#)); (iii) examining the transitional behavior of the turbulent flow, by systematically varying the downstream viscous and the upstream roughness length-scales; (iv) elaborating on the existing statistical picture of similar turbulent flows, as painted by laboratory experiments, using turbulence stresses, quadrant analysis and energy spectra; and (v) visualizing instantaneous fluctuating flow fields to complement these statistical measures.

## 2. Simulation preliminaries

The incompressible Navier-Stokes equations,

$$\frac{\partial u_i}{\partial x_i} = 0, \quad (2.1)$$

$$\frac{\partial u_i}{\partial t} + \frac{\partial u_i u_j}{\partial x_j} = -\frac{1}{\rho} \frac{\partial p}{\partial x_i} + \nu \frac{\partial^2 u_i}{\partial x_j^2}, \quad (2.2)$$

are solved by the fractional time-step method described in [Pierce & Moin \(2004\)](#). In (2.2)  $u_i = \{U, V, W\}$  are the instantaneous velocities in the streamwise, wall-normal and spanwise directions ( $x, y, z$ ), respectively,  $p$  is the pressure and  $\nu$  is the kinematic viscosity. In this study, the superscript ' is used to identify the fluctuating component and an over-bar will be used to signify the mean value of various turbulence statistics. The algorithm employs finite-differences on a three dimensional, staggered, Cartesian mesh. Second-order central differences are used for all spatial derivatives. The discrete equations are advanced in time by a semi-implicit scheme based on Newton-Raphson iterations, which is second-order accurate.

The computational domain is divided into two sections: an initial rough-wall section of length  $L_{rs}$  is followed by a smooth-wall section. A schematic is provided in figure 2. Square cylindrical ribs of height  $k$  are placed on the bottom, rough-wall, while the upper wall is kept smooth. The geometry of the rough wall is similar to the fully developed rough-wall simulations by [Ikeda & Durbin \(2002, 2007\)](#) and [Leonardi et al. \(2003\)](#). Following [Ikeda & Durbin \(2007\)](#), the spacing between successive roughness elements is  $w/k = 9$ . This spacing is sufficiently wide to ensure  $k$ -type roughness, while providing near-maximum form-drag. A recycling plane is used to generate a fully developed rough wall in the initial section, of length  $L_{fdr}$ , and to establish realistic turbulent inflow conditions to the smooth section. This recycling plane can, alternatively, be thought of as the inflow plane for the subsequent, downstream developing, channel flow. The procedure involves extracting an instantaneous cross-flow plane of the velocity field at

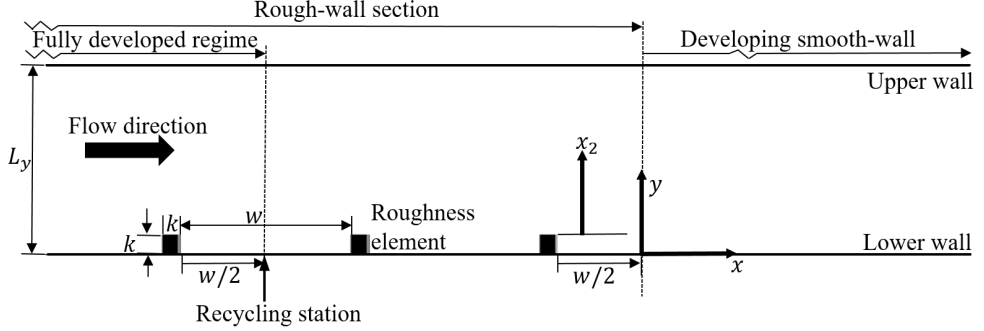


Figure 2: Computational domain and coordinate system. Spanwise ( $z$ ) direction is outward from the figure.

the streamwise recycling station and applying it at the inflow. The inflow mass flow rate is maintained constant at every time step.

Four test cases have been simulated, all of which have identical streamwise and wall-normal extents of the domain, which are  $L_x = 15.83\delta$  and  $L_y = 2.00\delta$ . The spanwise domain size for the low-Reynolds-number case is  $L_z = 1.96\delta$ , and for the high-Reynolds-number cases  $L_z = 2.08\delta$ . Additional parameters are summarized in table 1. These test cases are primarily differentiated by their  $\delta/k$  ratio and by their bulk Reynolds number,  $Re_b = U_b\delta/\nu$ , where  $U_b$  is the bulk velocity.

The initial, fully developed, rough-wall regime includes enough roughness elements within its length,  $L_{fdr}$ , for the near-wall, streamwise two-point correlations to become low at large streamwise separations. Ikeda & Durbin (2007) and Leonardi *et al.* (2003) both had four roughness elements for their fully developed rough-wall simulations, which is around half the number we have used for any of our test cases. Two roughness cavities after the recycling station were found adequate to provide a short, yet naturally developing evolution between the initial fully developed rough-wall regime and the developing, smooth-wall regime. The difference in the mean reattachment lengths of the primary re-circulation region between the last roughness element and a roughness element in the fully developed rough regime was about 5%. The spanwise domain is sufficiently wide to avoid spurious correlation in that direction. Figure 3, for case B, shows the normalized two-point correlations of the fluctuating velocities,

$$R_{\alpha\alpha}^z(x, z) = \frac{\overline{\alpha'(x, z)\alpha'(x, z + \Delta z)}}{\overline{\alpha'\alpha'}}, \quad (2.3)$$

where  $\alpha = (u, v, w)$ . The two figures are in the near-wall region, at the center of a cavity in the fully developed rough-wall region, and at  $x/\delta = 5.0$  in the developing, smooth-wall region. The drop of these two-point correlations to levels close to zero indicates that the spanwise domain size is adequate.

Jimnez (2004) recommended a  $\delta_b/k > 40$  for similarity laws to appear in turbulent rough-wall boundary layers, where  $\delta_b$  is the 99% boundary layer thickness. Many earlier laboratory experiments and all direct simulations have used smaller values (e.g. Cheng & Castro 2002; Ikeda & Durbin 2007; Orlandi *et al.* 2006). Some recent physical experiments have exceeded the criterion (Volino *et al.* 2011; Squire *et al.* 2016). Here, we assume the channel half-height  $\delta$  and  $\delta_b$  are equivalent. For their square-rib simulations Leonardi *et al.* (2003) and Miyake *et al.* (2002) used  $\delta/k = 5$ , while Ikeda & Durbin (2007) used  $\delta/k = 8.5$ . Ashrafiyan *et al.* (2004) used a higher ratio of  $\delta/k \approx 30$ , but

Table 1: Summary of simulation parameters.

Case	$Re_b$	Number of grid points	$\delta/k$	$L_{rs}/\delta$	$L_{fdr}/\delta$
A	4000	$1900 \times 326 \times 192$	12.0	7.50	5.83
B	18000	$2280 \times 379 \times 288$	12.0	7.50	5.83
C	18000	$2280 \times 374 \times 288$	16.0	7.50	5.63
D	18000	$2280 \times 396 \times 288$	9.6	8.33	6.25

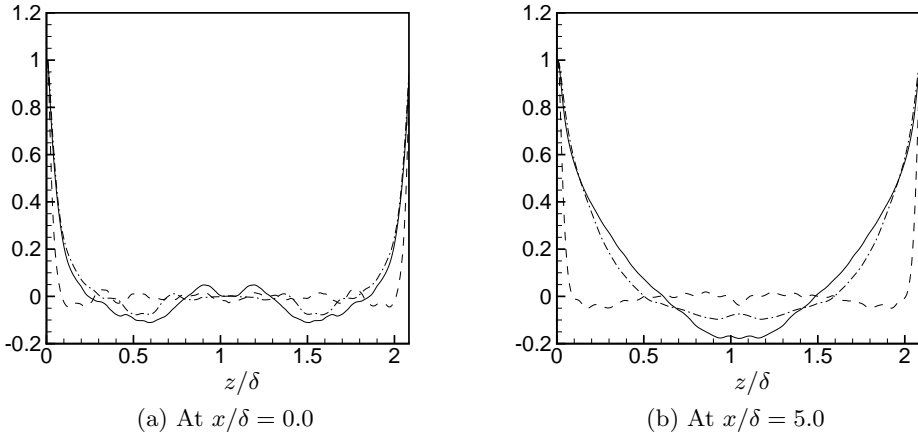


Figure 3: Two-point correlations of fluctuating velocities in the spanwise direction at  $y/\delta = 0.060$  for case B. —  $R_{uu}^z$ , - - -  $R_{vv}^z$  and - · - ·  $R_{ww}^z$ .

Table 2: Spatial and temporal resolutions for the RTS cases. The normalization is with the friction velocity at the upper smooth wall in the fully developed rough-wall region,  $u_{\tau S}$ .

Case	$\Delta x_s^+$	$\Delta z_s^+$	$\Delta y_s^+ _{min}$	$\Delta y_s^+ _{max}$
A	2.35	3.01	0.179	2.46
B	7.73	8.05	0.436	7.65
C	7.60	7.92	0.429	7.52
D	8.04	8.38	0.454	7.95

their simulations were only transitionally rough. Nagano *et al.* (2004) used three different ratios,  $\delta/k = 5, 10$  and  $20$ . Although they did not directly report their effective sand-grain length scales, by using the reported  $k^+$  we infer that  $\delta/k = 20$ , and that the flow was only transitionally rough. It should be noted that a higher  $\delta/k$ , although desirable, reduces the effective sand grain roughness  $r^+$  for a given bulk Reynolds number,  $Re_b$ . The present choices of  $\delta/k = 9.6, 12$  and  $16$ , are larger than those used by most previous DNS studies, and ensure that the rough-wall falls in the fully-rough regime, i.e  $r^+ > 90$  (see Durbin & Reif 2011). In this fully-rough category, if the roughness geometry is fixed, the flow becomes independent of  $\nu$ ; or, the friction velocity on the rough-wall  $u_{\tau R}$  becomes independent of  $Re_b$ .

Following Antonia & Luxton (1972), the start of the developing, smooth-wall regime

Table 3: Approximate maxima of local grid spacing normalized by the local Kolmogorov lengthscale  $\eta = (\nu^3/\epsilon)^{0.25}$  for the RTS cases.

Cases	$\Delta x/\eta _{max}$	$\Delta z/\eta _{max}$	$\Delta y/\eta _{max}$
A	5.2	6.4	1.7
B, C and D	10.6	10.9	4.6

( $x = 0$ ) is located at a distance  $w/2$  after the last roughness element. This origin is located downstream of the primary re-circulation zone following the last roughness element. Also such a choice means that the rough-wall section has an integer number of roughness-cavities of equal size. For each roughness-cavity the skin friction is calculated using both form drag and viscous drag, whereas in the developing smooth-wall section skin friction is simply the viscous drag.

The no-slip condition is applied on the upper and lower walls. Periodic boundary conditions are used in the spanwise direction and the convective outflow condition  $\partial u_i/\partial t + c\partial u_i/\partial x = 0$  is applied at the outlet boundary, where  $c$  is the local bulk velocity. Uniform grid spacing is used in the streamwise and spanwise directions, while a non-uniform grid is used in the wall-normal direction, with mesh clustering near the bottom wall, near the top of the roughness elements and near the upper smooth wall. About 75 grid points are nestled below  $y/\delta = 0.10$  for all three high Reynolds number cases. Stringent restrictions on the spatial resolution are imposed by the initial rough-wall section. The spatial resolutions in the present simulations (see table 2) are comparable to those used by Ikeda & Durbin (2002, 2007), and are better than those adopted for the cube-roughened turbulent flow simulations by Leonardi & Castro (2010). Table 3 shows local spatial resolution maxima of about  $10\eta$ , which occurs near the corners of the roughness elements. Although the calculation of  $\eta$  is a function of  $\epsilon$ , which itself depends on the resolution, the Kolmogorov lengthscale provides an additional measure of grid adequacy, along with the viscous scaling of the grid spacing (table 2). For the majority of the domain, particularly in the developing smooth-wall regime, the maximum local spatial spacing of grid cells lies within a couple of Kolmogorov lengthscales. The simulations are initially advanced for about  $50\delta/U_b$  time-units to drive out the transients, after which the calculation of statistics begins and carries on for an additional  $450\delta/U_b$  time-units.

### 3. Results

#### 3.1. Validation

An extensive validation study was carried out to build confidence in the accuracy the simulations. Results from three validation cases are presented in figure 4. One is the low-Reynolds-number, fully developed, smooth-wall channel flow DNS by Moser *et al.* (1999), at  $Re_\tau = 180$ . The other two have the same  $Re_b$  and a wall-normal domain extent of  $L_y = 2\delta + k$ , and are taken from Orlandi *et al.* (2006). The first of these involves  $k$ -type roughness with  $\delta/k = 5$  and  $w/k = 7$ , while the second has  $d$ -type roughness with  $w/k = 1$  and the same  $\delta/k$  ratio.

Excellent agreement is obtained with reference data for the smooth-wall channel flow. For the rough-walls a very good agreement is achieved with  $\bar{u}$  and  $\nu\partial\bar{u}/\partial y$  as well. However, higher turbulence shear stress  $\bar{u}'v'$  values are observed near the top of the roughness-elements than were seen by Orlandi *et al.* (2006). It is unclear why this

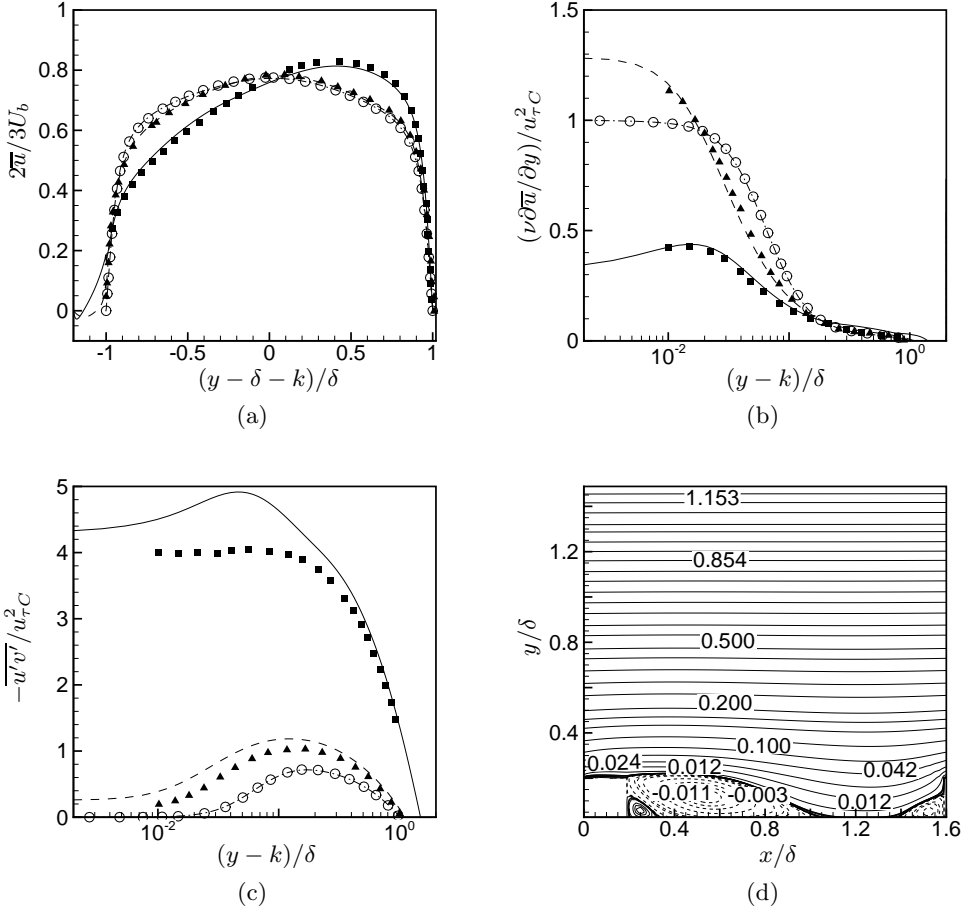


Figure 4: Validation profiles for fully developed channel flows: variation in the wall-normal direction of (a) mean streamwise velocity  $\bar{u}$ , (b) wall-normal mean velocity gradient  $\nu \partial \bar{u} / \partial y$ , and (c) turbulence shear stress  $\bar{u}'v'$ . — rough-wall flow with  $w/k = 7$  and  $k/\delta = 0.2$ , - - - rough-wall flow with  $w/k = 1$  and  $k/\delta = 0.2$ , and - · - · smooth-wall channel flow with  $k/\delta = 0$ . (d) Mean streamlines for the rough-wall flow with  $w/k = 7$  and  $k/\delta = 0.2$ . In these figures  $u_{\tau C}$  is the friction velocity at the wall for the smooth-wall channel flow. Filled-symbols: data from [Orlandi et al. \(2006\)](#) and open-symbols: data from [Moser et al. \(1999\)](#). Triangles represent  $d$ -type and squares represent  $k$ -type roughnesses.

difference occurs, but it should be noted that the present simulations have better resolved computational grids, particularly in the wall-normal direction near the bottom-wall and near the roughness-element height. The streamlines for the  $k$ -type roughness case in figure 4d demonstrate all the essential mean-flow features observed in [Ikeda & Durbin \(2007\)](#) and [Leonardi et al. \(2003\)](#). Among them are the primary separation bubble downstream of the roughness-element, a small positive re-circulation region nestled between the roughness-element and the primary separation bubble, a small separation bubble upstream of the roughness-element, and another thin separated film above the roughness-element with reattachment just before its trailing edge. The reattachment

Table 4: Parameters obtained in the fully developed regime. Here the roughness Reynolds number  $k^+ = u_{\tau R} k / \nu$ .

Case	$k^+$	$D_p$	$D_v$	$r/\delta$	$r^+$	$Re_{\tau S}$	$M$
A	42	0.0161	-0.000875	0.694	343	284	3.94
B	185	0.0158	-0.000609	0.694	1540	1115	5.10
C	132	0.0145	-0.000607	0.521	1105	1090	4.81
D	254	0.0188	-0.000614	0.868	2105	1160	5.32

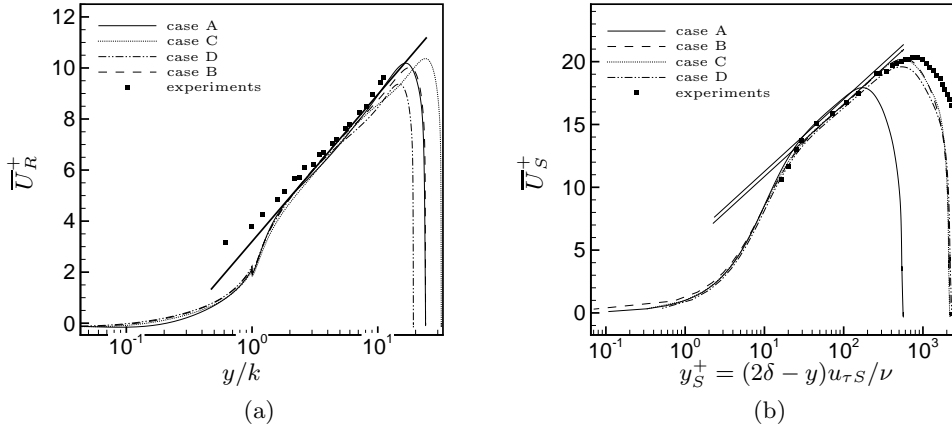


Figure 5: (a) Inner-scaled rough-wall mean streamwise velocity  $\bar{U}_R^+$  profile in the fully developed regime. The straight line is given by:  $\bar{U}_R^+ = (1/0.40)\ln(y/k) + 3.2$ . (b) Inner-scaled upper smooth-wall mean streamwise velocity  $\bar{U}_S^+$  profile in the fully developed regime. The straight lines are given by:  $\bar{U}_S^+ = (1/0.40)\log(y_S^+) + C$ . The additive constant  $C$  are 5.1 and 5.5. Symbols: experiments by [Hanjalic & Launder \(1972\)](#).

length of the primary separation bubble is  $4.7k - 4.8k$  from the trailing edge of the roughness element. The secondary separation starts at about  $-1.5k$  from the leading-edge of the roughness-element. These compare favorably with the values of  $\sim 4.8k$  and  $-1.5k$  reported by [Leonardi et al. \(2003\)](#). Additionally, another case from [Leonardi et al. \(2003\)](#) with spacing similar to that used in present test cases ( $w/k = 9$  and  $L_y = 2\delta$ ) was simulated. The computed form-drag was  $\sim 0.0122$ , within 3% of the value inferred from their figure 9.

### 3.2. Fully developed regime

Figure 5 shows the inner-scaled mean streamwise velocity profiles at both the bottom rough wall and the upper smooth wall, in the fully developed regime. Hot-wire measurements by [Hanjalic & Launder \(1972\)](#) are also shown. The experimental data were obtained at the same  $w/k$  as in the present work — albeit one with a comparatively small  $\delta/k = 8.5$ . These measurements were taken at a Reynolds number of  $Re_{U_{max}} = U_{max}\delta/\nu = 35,500$ , where  $U_{max}$  is the maximum mean velocity. Above both rough and smooth walls, and within the log-law region, the comparison with the DNS results is favourable. The displacement to the right in figure 5b is a result of a higher  $Re_{\tau S}$  for

the lab experiments, and the small overshoot is more likely due to a smaller  $\delta/k$  ratio. The non-dimensional friction velocity on the bottom rough-wall  $u_{\tau_R}$  is computed from the viscous drag

$$D_v = (\nu/U_b^2)(1/L_{fdr}) \int_0^{L_{fdr}} (\partial \bar{U}/\partial y)|_{y=y^h} dx$$

on the bottom wall and top of the roughness elements (the height of these two different types of no-slips surfaces is indicated here by  $y = y^h$ ) plus the form drag

$$D_p = (1/\rho U_b^2)(1/L_{fdr}) \sum_{n=1}^N \int_0^k (\bar{P}_f - \bar{P}_b) dy$$

due to the pressure difference across these discrete roughness elements:  $u_{\tau R}^2 = D_p + D_v$ . In the expression for  $D_p$ ,  $N$  is the number of roughness elements in the fully developed regime, and  $\bar{P}_f$  and  $\bar{P}_b$  are mean pressure values on the front and back of the roughness elements. Details on the parameters obtained in the fully developed regime are listed in table 4. For test cases A and B the two  $u_{\tau R}$  values are within 0.6% of each other, thus demonstrating their fully-rough nature. The contribution of  $D_v$  is only a very small fraction of the entire  $u_{\tau R}^2$  — 5.7% for case A, 3.9% for case B, 4.4% for case C and 3.3% for case D. The form drag contribution,  $D_p$ , is essentially the same for cases A and B, which have the same  $\delta/k$ ; whereas  $D_v$  shows an approximately 30% change for the high  $Re_b$  simulations. Also, the net contribution of  $D_v$  is negative due to the mean separation bubbles forming behind and in front of the roughness elements.

The effective sand-grain roughness,  $r$ , is estimated as  $r = k \exp[-\kappa(B - 8.5)]$ , where  $B$  is the wall-intercept of the log-law, fitted to the inner-scaled mean streamwise velocity profiles. The value of  $B = 3.2$  is the same as found by [Ikeda & Durbin \(2007\)](#) and [Hanjalic & Launder \(1972\)](#). For our test cases  $r/k = 8.33$ , which is comparable to the ratio obtained by [Volino et al. \(2011\)](#) for their boundary layer lab experiments, involving small square bars. The effective sand-grain roughness is a significant fraction of the channel half-height ( $r = 0.694\delta$ ); however,  $r$  is merely a parameter that equates the log-layer displacement with the experiments by [Nikuradse \(1933\)](#). [Ikeda & Durbin \(2007\)](#) obtained an effective sand-grain roughness length of  $r = 1.09\delta$  for their rib-roughened channel flow simulations.

The upper, smooth wall establishes a log-law region with wall-intercepts of  $C = 5.5$  and  $C = 5.1$  as shown in figure 5b. These are similar to intercepts measured in fully developed smooth-wall channel flows of comparable  $Re_b$ . But the friction velocity at this wall,  $u_{\tau S}$ , is higher than equivalent fully developed smooth-wall channel flows, which signals the interaction between the two walls.

We can define a roughness sublayer (RS) that is dynamically influenced by the underlying rough wall, and that is spatially inhomogeneous. For case B, as shown in figure 6, the extent of this RS can be identified as the wall-normal distance from the lower wall where horizontal inhomogeneity in the mean velocity disappears. It is at  $y/k \approx 4.5$ ; for other cases too, this height is between  $y/k = 4$  and 5. Additionally, it is noticeable from figures 5a and 6 that the fitted log-law enters the RS, extending down to about  $y \approx 2k$ . [Ikeda & Durbin \(2007\)](#) used the onset of the fitted log-law for mean velocity and  $P/\epsilon \approx 1$  to identify their roughness sublayer height as  $y \approx 2k$ , where  $P$  and  $\epsilon$  are the production and dissipation rates of the turbulence kinetic energy.

Above smooth-wall boundary layers, [Wei et al. \(2005\)](#) defined the onset of the log-law region,  $y_I$ , as the wall-normal location where viscous forces lose dominance. Using the mean-momentum budget terms, they showed that  $y_I$  occurred just above the vertical

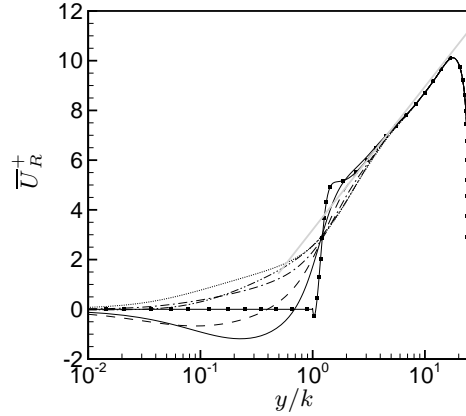


Figure 6: Inner-scaled mean streamwise velocity at different streamwise positions in the fully developed rough-wall regime for case B. — fitted log-law profile, — at  $s/k = 1.13$ , - - - at  $s/k = 2.80$ , - - - - at  $s/k = 4.50$ , ····· at  $s/k = 6.25$ , - - - - - at  $s/k = 7.80$  and —■— at  $s/k = 9.50$ . The straight line is given by:  $\overline{U}_R^+ = (1/0.40)\ln(y/k) + 3.2$ .  $s$  is distance from the trailing edge of a roughness element.

location of the maxima of turbulence shear stress, at  $y_m$ . For rough-wall boundary layers, Mehdi *et al.* (2013) proposed  $y_I = C_I y_m$ , with  $C_I \sim \mathcal{O}(1)$ . Their argument was based on qualitative similarity of mean dynamics with smooth-wall flows in the zone where transition to the log-law region takes place. They further proposed functions of the following form for estimating  $y_m$ :

$$y_m = C_m (\nu/u_\tau)^a r^b \delta^c.$$

Here,  $C_m, a, b$  and  $c$  are empirically determined constants based on three different classification regimes of  $y_m/r$ . Using their function for  $y_m/r < \mathcal{O}(1)$ , for case B,  $y_m \approx 1.18k$ , which is close to the exact location at  $y_m = 1.25k$ . Based on this estimate of  $y_m$  and the above mentioned approximate location for the onset of the log-law region, at  $y \approx 2k$ ,  $C_m \approx 1.70 \sim \mathcal{O}(1)$ .

Following Andreopoulos & Wood (1982) the hydrodynamic roughness length-scales can be used to compute the strength of roughness step  $M = \ln(z_r/z_s)$  in order to quantify the degree of perturbation for these RTS simulations. Here,  $z_r = r \exp(-8.5\kappa)$  is the hydrodynamic roughness length-scale in the fully developed rough-wall regime, and  $z_s = (\nu/u_\tau) \exp(-\kappa C)$  is an equivalent roughness length-scale from a separate fully developed smooth-wall channel flow at the same  $Re_b$ . The expression for  $z_s$  is derived by equating the log-law in terms of viscous length-scale,  $\delta_\nu = \nu/u_\tau$ , to an equivalent log-law in terms of a hydrodynamic roughness length-scale,  $z_s$ . Values of  $M$  given in table 4 are comparable to  $M = 3.4$  and  $5.1$ , reported by Hanson & Ganapathisubramani (2016). Hosni & Coleman (1993) reported  $M = 3.15$  for their RTS boundary layer experiments. It should be noted that, for cases A and B, the difference in  $M$  is due to different downstream lengthscales,  $\delta_v$ , and the difference in  $M$  between cases B, C and D is due to different upstream lengthscales,  $r$ .

### 3.3. Skin friction

The skin-friction coefficient  $C_f = (\nu/2.25U_b^2)(\partial \overline{U}/\partial y)$  in the developing, smooth-wall

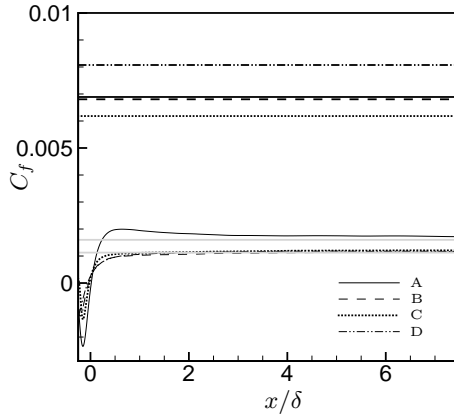


Figure 7: Skin friction,  $C_f$ , profiles in the developing, smooth-wall regime. Bold, black lines: fully developed rough-wall regimes, ——— fully developed smooth-wall channel flows.

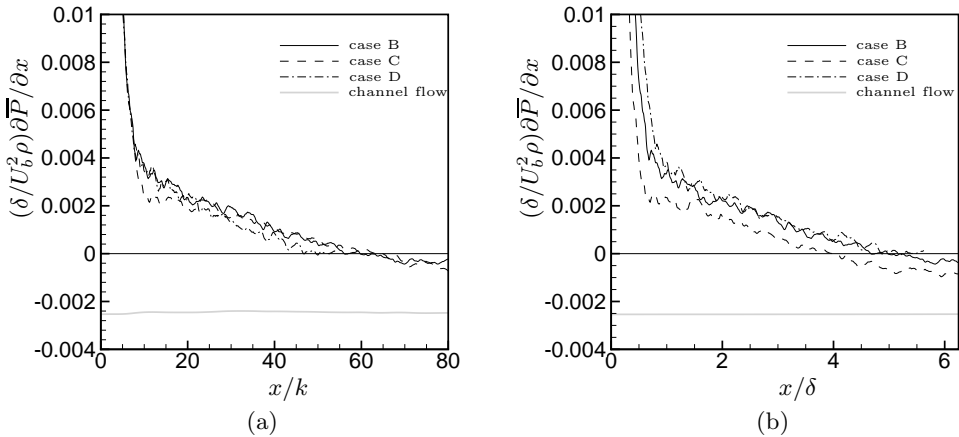


Figure 8: Streamwise variation of  $(1/\rho)\partial\bar{P}/\partial x$  at the lower wall in the developing regime, with  $x$  scaled by (a) the roughness length-scale,  $k$ , and (b) the channel half height,  $\delta$ .

regime is plotted in figure 7. It first reduces sharply, to levels well below the fully developed smooth-wall levels (gray lines) before growing quickly and then gradually leveling off (immediately after the step change in roughness, it becomes negative due to the separation bubble following the last roughness element). The skin friction profiles above the rough wall in figure 7 include contributions from both viscous and form drags. By  $x \approx 2\delta$ , the high-Reynolds-number cases plateau very close to fully developed smooth-wall levels. It would, however, be misleading to conclude that the  $C_f$  has equilibrated. Its incomplete recovery is more evident for the low-Reynolds-number case. Close inspection of  $(1/\rho)\partial\bar{P}/\partial x$  at the wall, shows that it is adverse over most of the domain, becoming negative near the end of the domain (figure 8). Preliminary results, not included here, from RTS simulations using cube roughness evidence this same behaviour.

Case A shows a steeper increase of  $C_f$  compared to the other cases, which is consistent

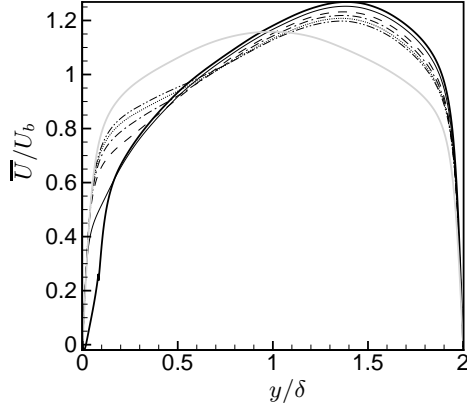


Figure 9: Outer scaled mean streamwise velocity  $\bar{U}/U_b$  in the developing section scaled from the lower wall for case A. ——— in the fully developed rough-wall regime, ——— at  $x/\delta = 0.42$ , ——— at  $x/\delta = 2.08$ , ——— at  $x/\delta = 3.75$ , ······ at  $x/\delta = 5.42$ , ——— at  $x/\delta = 7.08$ , ——— from fully developed smooth-wall channel flow.

with observations made by [Antonia & Luxton \(1972\)](#). The initial recovery of  $C_f$  is different for the three cases at high Reynolds numbers; they do not collapse when the streamwise distance is normalized by either  $\delta$  or  $k$ . However, the initial response of  $(1/\rho)\partial\bar{P}/\partial x$  at the wall does collapse when plotted against  $x/k$  (figure 8a), but not when the streamwise distance is scaled by  $\delta$  (figure 8b). This implies that, for the type of the roughness considered and for initial recovery the response of the pressure gradient at the wall can be extrapolated to large  $x/k$ , to estimate the streamwise distance required to reach the fully developed, smooth-wall gradient. A non-linear regression fit, using a disaccociation curve ([Hill 1913](#)), estimates this distance as  $x \approx 450k$  (or  $37\delta$ ).

### 3.4. Mean velocity

After the step change in roughness the retarded mean flow above the rough-wall experiences strong near-wall acceleration as shown in figure 9 for case A. By conservation of mass-flow rate, this is compensated by deceleration further away from the bottom wall, and both acceleration and deceleration gradually decrease in magnitude with downstream distance. By the last streamwise station in figure 9, at  $x/\delta = 7.1$ , the mean velocity has not recovered to the fully developed smooth wall profile, which is the symmetric gray curve.

The point of intersection between two successive and equally spaced streamwise stations from figure 9 has been used as an indicator of the ‘internal layer’ height ([Antonia & Luxton 1972](#)). It moves away from the wall with downstream distance. However, the consequent mean flow deceleration above these points of intersection is evidence that, for such internal flows, the entire wall-normal domain is affected by the change in roughness, and the idea of an internal boundary layer is not pertinent. Figure 10 shows the mean velocity profiles in the developing smooth-wall regime for the three high-Reynolds number cases. The profiles in outer variables are very similar. A hyperbolic-decline curve was fitted to the downstream decay of the outer peak of  $\bar{U}$ . For case B, it estimates the streamwise distance needed to reduce to fully developed, smooth-wall channel flow levels as  $x = 55\delta$ .

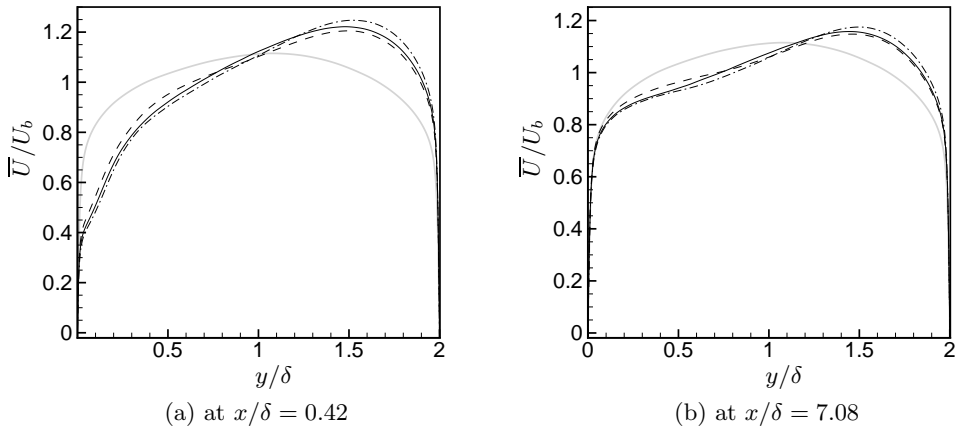


Figure 10: Outer-scaled mean streamwise velocity  $\overline{U}/U_b$  at different streamwise stations for the high-Reynolds-number cases. — case B, - - - case C, - · - - case D, and — from fully developed smooth-wall channel flow.

The inner-scaled mean velocity  $\overline{U}^+$  in the developing smooth-wall regime is shown in figure 11a for case B. Like the outer-scaled velocity profiles, it too shows quick initial recovery, but a fully developed, smooth wall profile has not developed by the domain exit. In the fully developed rough-wall regime, mean velocity levels are well below and towards the right of the developing regime profiles, due to the higher to high friction velocity  $u_{\tau R}$ . Very close to the bottom-wall ( $y^+ \leq 20$ ) nearly complete recovery and good collapse of the profiles with smooth-wall channel flow occurs by the end of the domain.

By the second streamwise station, at  $x = 2.08$  in figure 11a,  $\overline{U}^+$  has attained a qualitative shape that remains essentially unchanged and gradually shifts upwards with downstream distance. This slow upward shift is contrary to the trend observed by [Hanson & Ganapathisubramani \(2016\)](#). With downstream fetch, their profiles were initially pushed up, well above the smooth wall level (a consequence of low  $u_\tau$ ) and then settled down toward it. The mean velocity results in our initial strong non-equilibrium zone, between  $0 < x/\delta < 0.5$ , are plotted in figure 11b, and demonstrate this decay trend — but only at short distances where  $C_f$  is increasing.

Using these inner-scaled plots, it might seem interesting to investigate the existence of a log-law region in the transitional regime and possibly to fit log-law profiles. Marusic *et al.* (2013), for high Reynolds number, fully developed, smooth-wall boundary layers, provided empirical functions for the bounds of the log-law region:  $y_T^+ = 3\sqrt{Re_\tau}$  for lower onset location and  $y^+ = 0.15Re_\tau$  for the upper bound, which for the current  $Re_\tau$  falls between  $90 \sim 140$ . After the first streamwise station in figure 11a, at the wall-normal height where a log-law might possibly exist, it might appear that  $\kappa$  is higher than typical levels of  $0.40 - 0.41$ . This is not a warranted conclusion; the impression of a modified  $\kappa$  above  $y^+ > 40 - 50$  in figure 11a is misleading. The large velocity deficit created by roughness persists with downstream distance. The warranted conclusion is that an equilibrium log-law has not established, even by the end of the computational domain.

By contrast, the upper, smooth wall remains near to equilibrium, as evidenced by negligible difference between the profiles at successive streamwise stations and by establishment of the conventional log-law profiles in figure 11c. The frictional Reynolds number at this wall  $Re_{\tau u} = u_{\tau} U \delta / \nu$  for case B shows less than 8% reduction, from 1.115 down

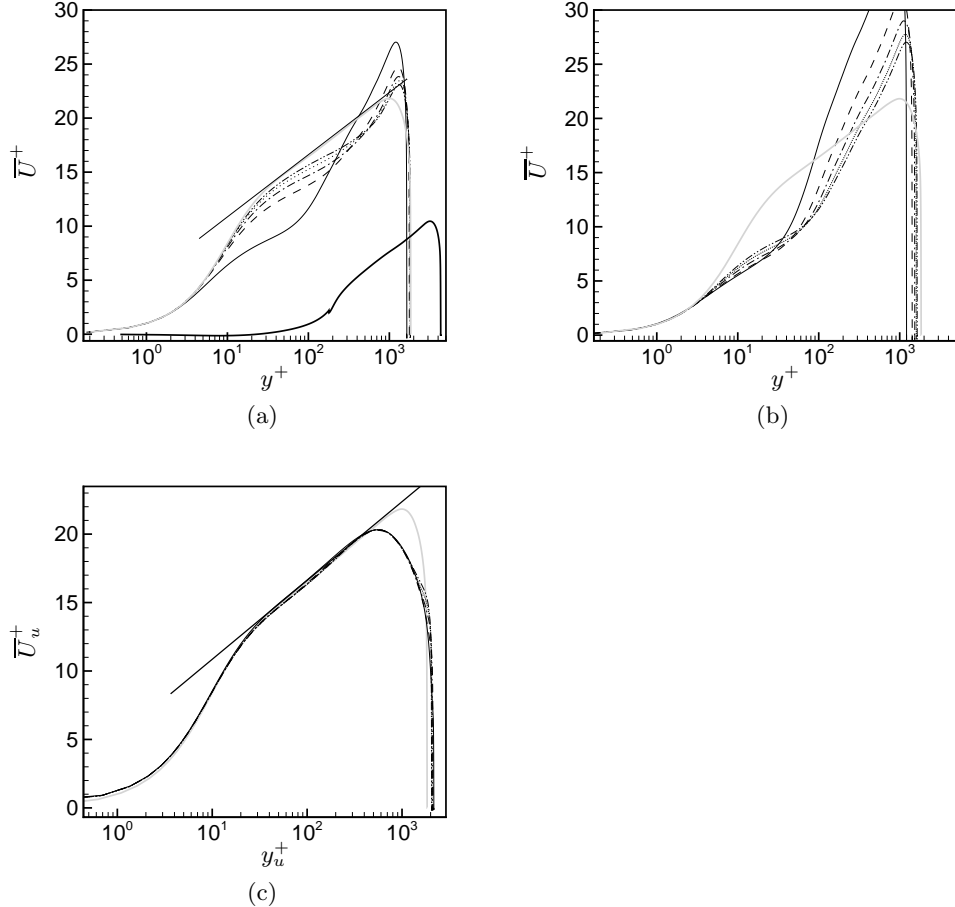


Figure 11: Mean streamwise velocity for case B in the developing, smooth-wall regime scaled from (a,b) the bottom wall and in inner coordinates,  $\bar{U}^+$  and  $y^+$ ; (c) the top wall and in inner coordinates,  $\bar{U}_u^+$  and  $y_u^+$ . (a,c) — in the fully developed rough-wall regime, — at  $x/\delta = 0.42$ , - - - at  $x/\delta = 2.08$ , - · - - at  $x/\delta = 3.75$ , ..... at  $x/\delta = 5.42$ , - · - - at  $x/\delta = 7.08$ , — from fully developed smooth-wall channel flow. (b) In the initial strongly non-equilibrium region with — at  $x/\delta = 0.08$ , - - - at  $x/\delta = 0.17$ , - · - - at  $x/\delta = 0.25$ , ..... at  $x/\delta = 0.33$ , - · - - at  $x/\delta = 0.42$ , — from fully developed smooth-wall channel flow.

to about 1.030, between the fully rough region and the last streamwise station. At the last measuring station in the developing regime the top wall shows an  $Re_\tau$  that is more than 10% higher than the fully developed smooth-wall channel flow, while on the more active, bottom wall,  $u_\tau$  has already recovered, as early as  $x = 2\delta$ . Although inner-scaled profiles are only presented for case B, the trends noted and conclusions drawn also apply to the other cases.

### 3.5. Turbulence stresses

Profiles of turbulence kinetic energy,  $K$ , and turbulence stresses in the developing smooth-wall regime are presented in figures 12 and 13. Plots in the fully developed

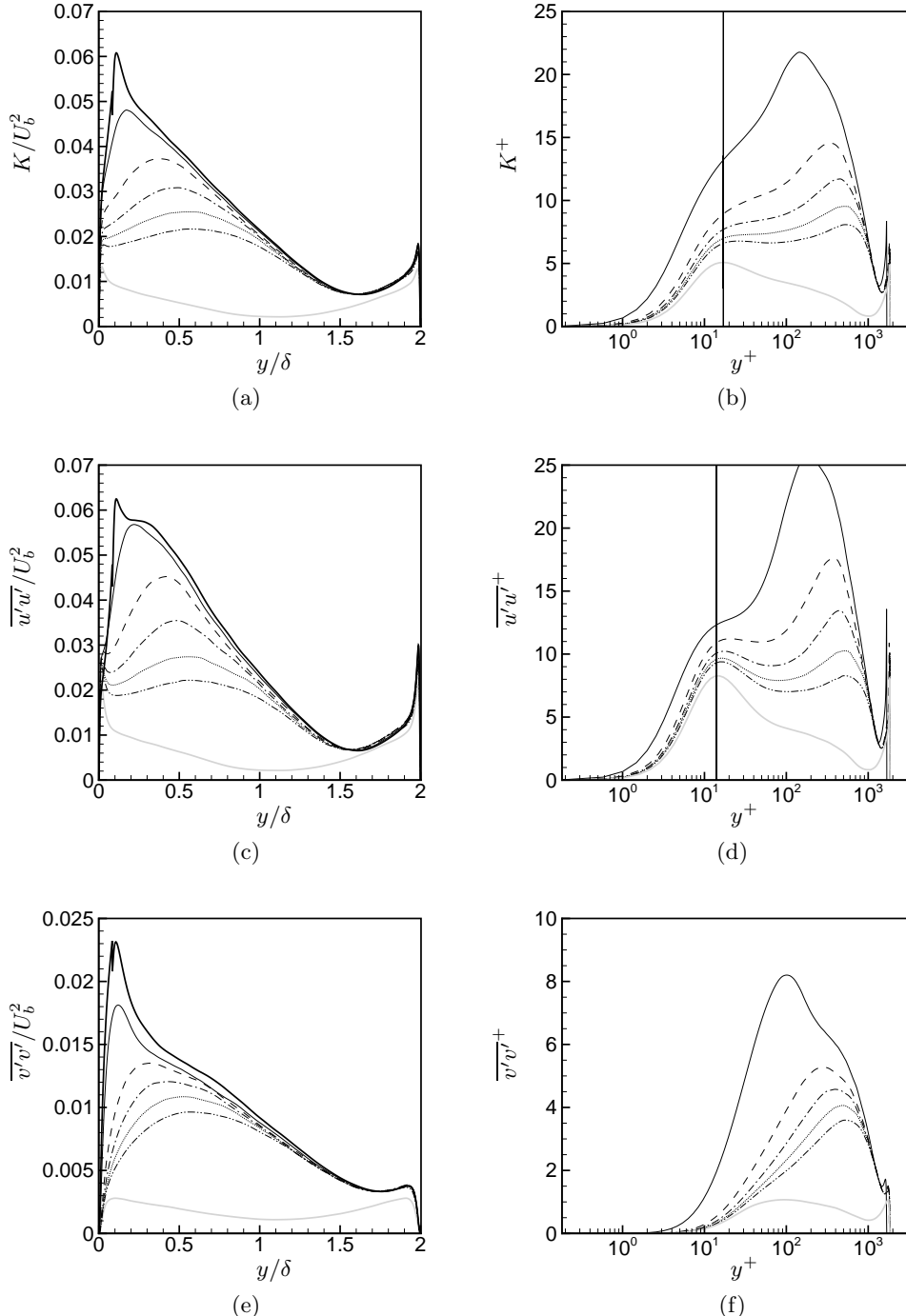


Figure 12: Normal turbulence stresses and TKE in the developing smooth-wall regime for case B. — in the fully developed rough-wall regime, — at  $x/\delta = 0.42$ , - - - at  $x/\delta = 2.08$ , - · - · - at  $x/\delta = 3.75$ , · · · · - at  $x/\delta = 5.42$ , - · - · - at  $x/\delta = 7.08$ , — from fully developed smooth-wall channel flow. (a,c,e) Using outer-scaled coordinates; (b,d,f) using inner-scaled coordinates. Vertical lines identify the location of inner peaks at  $y^+ = 17$  in (b) and  $y^+ = 14$  in (d).

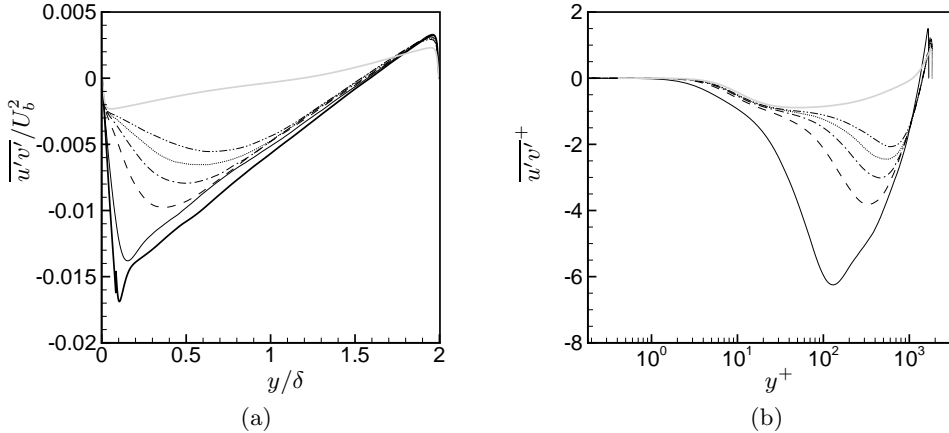


Figure 13: Turbulence shear stress in the developing smooth-wall regime for case B. — in the fully developed rough-wall regime, — at  $x/\delta = 0.42$ , - - - at  $x/\delta = 2.08$ , - - - - at  $x/\delta = 3.75$ , ..... at  $x/\delta = 5.42$ , - - - - - at  $x/\delta = 7.08$ , — from fully developed smooth-wall channel flow. (a) Using outer-scaled coordinates; (b) using inner-scaled coordinates.

regime exhibit a small discontinuity at  $y/k = 1$ . This is a result of the length of the streamwise averaging changing abruptly at the crests of the roughness elements. The wall-normal location of the outer-peaks of  $\bar{u}'\bar{u}'^+$  in the fully developed rough-wall regime stays virtually fixed at  $y/\delta \approx 0.11, 0.11, 0.084$  and  $0.13$  for cases A, B, C and D, respectively, which lies between  $y/k = 1.25$  and  $1.35$ . This is within the  $y/\delta = 0.05 - 0.2$  range observed for rough-wall boundary layers (Jimnez 2004; Jacobi & McKeon 2011). Using inner coordinates, the outer-peak for case B in the fully developed rough-wall regime is located at about  $y^+ = 600$ . The aforementioned range of  $y/k = 1.25 - 1.35$  also applies to the wall-normal location of the rough-wall peaks of  $\bar{u}'\bar{v}'^+$  for all four cases.

From all the plots, particularly those using outer scaling, over the developing smooth-wall, higher levels of turbulence, characteristic of the upstream rough-wall, persist to the domain exit. Outer peaks, attributable to the rough-wall, decay in magnitude with downstream distance, while being driven away from the lower wall. By the last streamwise station, these peaks are still vaguely discernible. However, despite this strong initial decrease and vertical transport, a very large mismatch remains with the fully developed smooth-wall profiles, shown by the light-gray curves in the figures.

By the second streamwise station in figure 12d, at  $x/\delta \geq 2.08$ , the wall-normal gradient of  $\bar{u}'\bar{u}'^+$  changes sign from positive to negative in vicinity of  $y/\delta \approx 0.02$ , indicating the establishment of a near-wall, inner peak. This inner peak is consistent with the near-wall of turbulent flow over smooth walls. Its wall-normal location shows negligible change with downstream distance. By the last streamwise station in figure 12d, the inner-peak magnitude is still about 10% higher than the fully developed, smooth wall level. Comments and observation made for the streamwise turbulence stress also apply to the turbulence kinetic energy (TKE), as is evident from figures 12a and 12b.

It is worthwhile to contrast the near-wall recovery of the streamwise turbulence stress with that of the outer flow. The near-wall region shows a strong initial recovery, with the profile shape closely matching that of the fully developed smooth-wall, after which there is only weak downstream reduction in magnitude. The outer-flow, on the other hand,

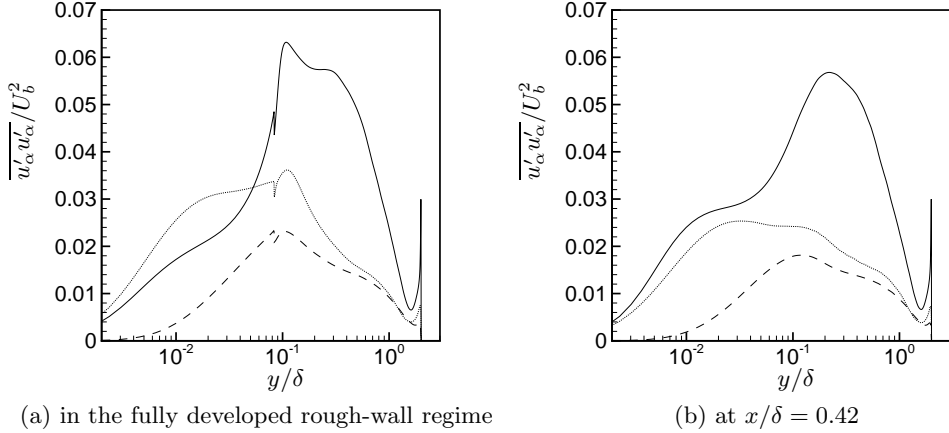


Figure 14: Normal turbulence stresses at fixed streamwise locations for case B. —  $\overline{u'u'}/U_b^2$ , — —  $\overline{v'v'}/U_b^2$  and .....  $\overline{w'w'}/U_b^2$ .

shows a stronger decay rate throughout the horizontal extent of the domain. It remains well above the asymptotic smooth wall profiles, which have a low level of turbulence in this region.

The turbulence wall-normal,  $\overline{v'v'}$ , and shear stress,  $\overline{u'v'}$  (figures 12e, 12f, 13a and 13b) present another interesting picture, with the fully developed smooth-wall counterpart having inner-layer peaks that lie further away from the wall. For our low-Reynolds-number case the peak of  $\overline{v'v'}$  lies at  $y^+ \approx 58$  and of  $\overline{u'v'}$  at  $y^+ \approx 34$ , while for the high-Reynolds-number case the two are located at  $y^+ \approx 105$  and  $y^+ \approx 53$ , respectively. At  $Re_\tau = 590$ , Moser *et al.* (1999) obtained peaks of  $\overline{v'v'}^+$  at  $y^+ \approx 78$  and of  $\overline{u'v'}^+$  at  $y^+ \approx 44$ . Since these peaks for wall-normal and spanwise turbulence stresses are further away from the wall than for  $\overline{u'u'}$ , their re-establishment is overshadowed by the higher turbulence magnitudes in the outer flow. This is especially true for  $\overline{v'v'}$ , where the near-wall peak is not established at all by the last streamwise station. The near-wall peak for  $\overline{u'v'}$ , however, appears to have formed by the second streamwise station, figure 13b, but it too is obscured by higher, outer-flow turbulence levels. As for the mean velocity data, discussed earlier, the upper-wall shows negligible downstream development, remaining similar to what is seen above the rough wall.

In the near-wall region for fully developed smooth-wall flows,

$$\overline{u'u'} > \overline{w'w'} > \overline{v'v'},$$

whereas for fully developed rib-roughened rough-wall flows

$$\overline{w'w'} > \overline{u'u'} > \overline{v'v'}.$$

Ikeda & Durbin (2007), who reported this particular precedence of turbulence stresses for rough wall flows, also noted that the 2-D, square ribs suppress the streamwise stress, which in turn enhances the spanwise motions. In our transitional regime, however, at the first streamwise station located downstream of the step change ( $x/\delta = 0.42$ ) the effect of upstream roughness elements on the near-wall turbulence anisotropy has already been lost and the normal stresses have re-attained their smooth-wall hierarchy:  $\overline{u'u'} > \overline{w'w'}$  (see figure 14). This is understandable because, once the roughness elements are removed,

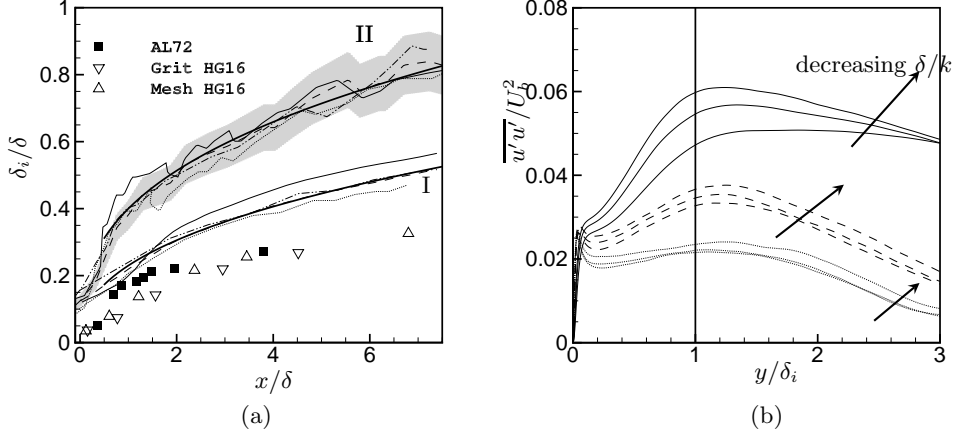


Figure 15: (a) IBL thickness profiles for RTS test cases; symbols: from lab experiments by Antonia & Luxton (1972) and Hanson & Ganapathisubramani (2016). — represents the fitted power laws:  $\delta_i/\delta \sim (x/\delta)^{0.41}$  for the set of profiles labelled I and  $\delta_i/\delta \sim (x/\delta)^{0.36}$  for the set of profiles labelled II. The grey envelope indicates the  $\pm 10\%$  extent for case B. — case B, - - - case C and ..... case D. (b) Profiles of  $\overline{u'u'}$  in the developing regime as a function of  $y/\delta_i$ . — at  $x/\delta = 0.42$ , - - - at  $x/\delta = 3.75$  and ..... at  $x/\delta = 7.08$ . — at  $y/\delta_i = 1.00$ .

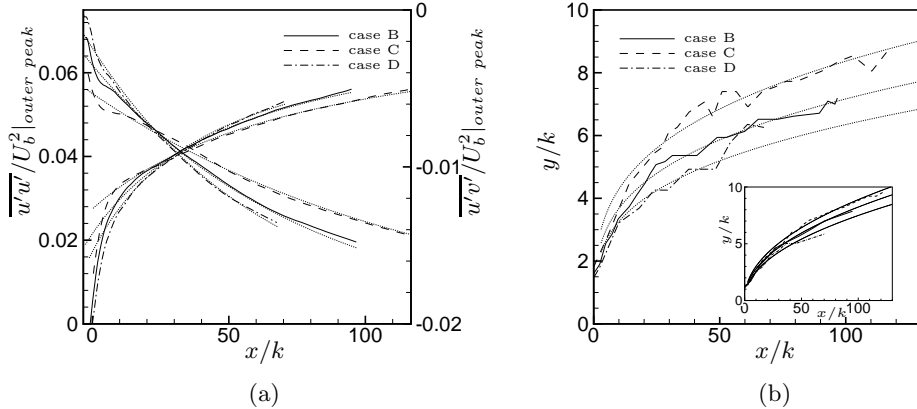


Figure 16: (a) Downstream variation of the outer peaks of  $\overline{u'u'}$  and  $\overline{u'v'}$  as a function of  $x/k$ . (b) Downstream growth of the wall-normal location,  $y/k$ , of  $\overline{u'u'}$  and  $\overline{u'v'}$  with  $x/k$ . ..... for both (a) and (b) represents profiles of approximate fitted functions.

the source for damping of streamwise turbulence motions disappears, allowing them to increase above the spanwise motions.

Although the role of the internal boundary layer (IBL) height,  $\delta_i$ , might not be apparent, its growth rate and utility as a length-scale for normalizing the wall-normal coordinate could prove instructive. Figure 15a shows the downstream variation of the IBL heights, which are defined as the wall-normal location where the developing, smooth-wall velocity first crosses the upstream, rough-wall mean-velocity profile. The fitted power

Table 5: Values of the unknowns in the interpolation functions for  $\gamma = a + b(\delta/k)$  and  $\theta = a + b(\delta/k)$ .

	$a$	$b$
$\gamma_{uu}$	0.0822	-0.00170
$\theta_{uu}$	-0.0263	0.00114
$\gamma_{uv}$	-43.9	-2.19
$\theta_{uv}$	-2.14	0.0728

law  $\delta_i \propto x^{0.41}$  agrees well with the trend of  $\delta_i \propto x^{0.43}$  reported by Antonia & Luxton (1972). Additionally, IBL profiles estimated by identifying the wall-normal location where  $\partial \bar{U} / \partial x$  vanishes (Antonia & Luxton 1972) are also shown in 15a and labelled II. The lack of smoothness in these IBL profiles is due to difficulty in discerning a precise location for  $\partial \bar{U} / \partial x = 0$ . Nonetheless, there does not appear to be a systematic difference in the growth rate for different test cases, and a major fraction of the profiles lie within the  $\pm 10\%$  envelope of case B. Compared to the experimental results in figure 15a, the present  $\delta_i$  are much larger. It should be pointed out that for channel flows, due to continuity, the entire wall-normal domain is affected by the step change in roughness. This is shown by mean flow acceleration near the lower wall and mean deceleration further away from it in figure 9.

Downstream development of  $\overline{u'u'}$  as a function of  $y/\delta_i$  is reported in figure 15b. Here, we use the first definition of IBL. No collapse of profiles is observed within the streamwise extent examined. The same was seen for other turbulence stresses. One concludes from the lack of collapse that  $\delta_i$  is not a similarity length-scale. Furthermore, it is misleading to construe  $\delta_i$  as a demarcator of a developing mean-flow region below an unaffected, upstream region. Rather, it should simply be regarded as a point where the developing mean velocity equals the velocity above the rough wall.

The behaviour of the outer peaks of the Reynolds stresses can be used to estimate the streamwise distance needed by the turbulence stresses to recover to near fully developed smooth-wall levels. Figure 16a shows the downstream decay of the outer peaks of  $u'u'$  and  $\overline{u'v'}$ . The decay with  $x/k$  is more severe when  $\delta/k$  is smaller. Approximate curve fits, for  $x > 10k$ , of the type

$$\frac{\overline{u'u'}}{U_b^2}|_{\text{outer peak}} = \gamma_{uu} e^{\theta_{uu}(x/k)}$$

for  $\overline{u'u'}$  and

$$\frac{\overline{u'v'}}{U_b^2}|_{\text{outer peak}} = \frac{1}{\gamma_{uv} + \theta_{uv}(x/k)}$$

for  $\overline{u'v'}$  have been added to the figure. The unknowns  $\gamma$  and  $\theta$  for these three high-Reynolds-number cases are fitted to the form,  $a + b(\delta/k)$ , and the values of  $a$  and  $b$  are listed in table 5. The downstream development of the wall-normal location,  $y/k$ , of these outer peaks of  $\overline{u'u'}$  is shown in figure 16b, while that of  $\overline{u'v'}$  is in the inset. Power law fits,  $(y/k) \sim (x/k)^m$ , have also been included in figure 16b; where  $m = 0.29$  for  $\overline{u'u'}$  and  $m = 0.47$  for  $\overline{u'v'}$ . Using these approximate functions, we can estimate that the outer peak of  $\overline{u'u'}$  for case B would require about  $250k$  (or  $20.8\delta$ ) of downstream distance to reach levels similar to those of fully developed smooth-wall channel flows. Rewriting the expression for the outer peaks of  $\overline{u'u'}$  as a function of  $x/\delta$ , instead of  $x/k$ , still results in the exponents displaying a decay rate inversely related to  $\delta/k$ , albeit one that

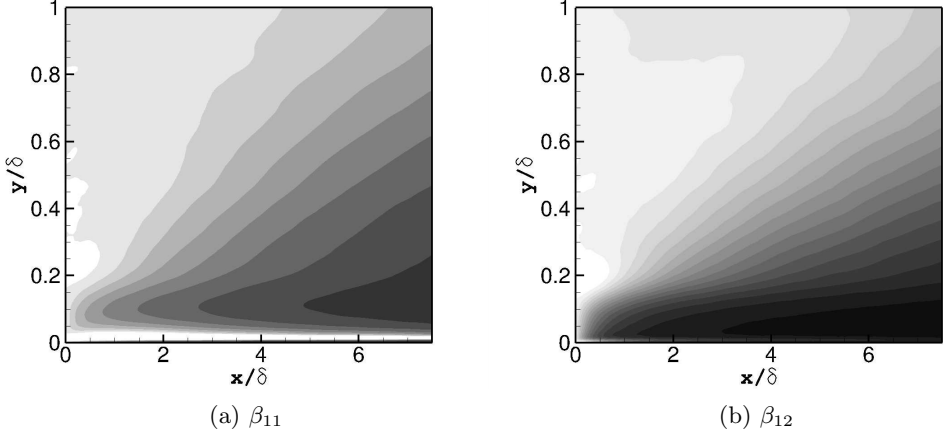


Figure 17: Normalized recovery magnitudes of turbulence stresses for case B. Scale: black 0.0, white 1.0.

is comparatively slower. This confirms the argument made earlier that the downstream response of the outer flow turbulence is directly influenced by the roughness size.

Let subscript  $R$  denotes values at the start of the smooth wall regime, and  $S$  denote fully developed, smooth-wall values. Then

$$\beta_{ij} = (\overline{u'_i u'_j} - \overline{u'_i u'_j}_S) / (\overline{u'_i u'_j}_R - \overline{u'_i u'_j}_S).$$

(Jacobi & McKeon 2011) measures the extent of recovery.  $\beta_{11}$  and  $\beta_{12}$  are contour plotted in figure 17. Darker contours are lower values of  $\beta$ , tending to black at the smooth wall value  $\beta = 0$ .

The presence of a large black patch for  $\overline{u'v'}$  close to the wall ( $y/\delta < 0.2$ ), but above  $y^+ = 40 \sim 50$ , indicates its swift recovery.  $\overline{u'v'}$  recovers more slowly. This, along with the results of energy spectra presented later in figure 21, supports the argument that large, inactive structures associated with  $\overline{u'v'}$  show a relative slow return to their fully developed smooth-wall characteristics. This is in contrast to the near wall, shear-stress producing motions responsible for  $\overline{u'v'}$ . The light-gray regions above about  $y/\delta = 0.2$  indicate the large deficit, high turbulence outer-flow zone, as seen previously in figures 12 and 13.

To further illustrate the comparatively quick near-wall recovery of shear producing motions, quadrant analysis (Wallace *et al.* 1972; Wallace 2016) is used to identify different components of  $u'v'$  that make up the averaged turbulent shear stress  $\overline{u'v'}$ . Events from all four quadrants in figure 18 show increased magnitude in the fully developed rough-wall regime. Quadrant 2 (Q2) and quadrant 4 (Q4) events account for negative  $\overline{u'v'}$  and, hence, positive production of TKE ( $P = -\overline{u'_i u'_j} \partial \overline{u}_i / \partial x_j$ ). They are, at least in absolute terms, the dominant events in all three regimes: fully developed rough wall, transitional, and fully developed smooth wall. Results for fully developed smooth walls are well documented in the literature (see Wallace 2016). In the transitional regime, by the last station, Q2 has recovered the most, followed closely by Q4, which is distinctly apparent from the normalized recovery contours given figure 19.

Coherent, instantaneous streamwise motions of alternating high and low momentum are characterized by a large positive and negative  $u'$ , while  $v'$  is smaller, often times by an order of magnitude. Occasionally, however, the low-speed streaks are slowly

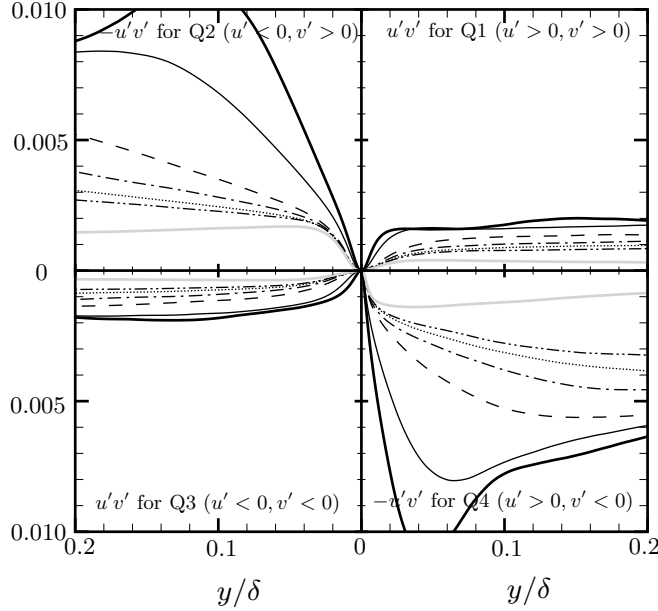


Figure 18: Quadrant analysis profiles of  $\overline{u'v'}$  for case B. — in the fully developed rough-wall regime, — at  $x/\delta = 0.42$ , - - - at  $x/\delta = 2.08$ , - · - · - at  $x/\delta = 3.75$ , ..... at  $x/\delta = 5.42$ , - · - · - at  $x/\delta = 7.08$ , — from fully developed smooth-wall channel flow.

lifted up, followed by a strong vertical transport away from the wall. This sequence of events was referred to as ‘bursting’ by [Kim et al. \(1971\)](#), and is followed by high-speed inward motions. These ejection and sweep events, due to their large, negative  $u'v'$  infusions, contribute to the dominance of quadrants 2 and 4. Events from both of these quadrants, according to figure 19, show a comparatively quick relaxation close to the wall. Furthermore, it is evident that in the fully developed rough-wall regime the roughness elements greatly enhance the near-wall turbulence activity, thus severely altering the profiles tracked by different quadrants, particularly Q2 and Q4. In the transitional regime, once these roughness elements disappear the source for this disruption vanishes as well, and the near-wall balance between Q2 and Q4 over smooth walls is re-established relatively quickly.

#### Turbulence scales

In the fully developed rough-wall regime, the production rate of TKE,  $P$ , in figure 20a manifests a single peak, just above the roughness elements, which coincides with the peaks observed in turbulence stresses earlier. Above the two-dimensional roughness elements and within the roughness sublayer, heterogeneities only manifest in the streamwise and wall-normal directions. Within this roughness sublayer, the contributions to  $P$  are only from terms with streamwise and wall-normal gradients of the mean velocity field. However, the fully developed, rough-wall profiles in figure 20, like other fully developed results presented earlier, incorporate streamwise averaging as well. The dissipation rate of  $K$  is of significantly larger magnitude than a fully developed smooth wall, both very

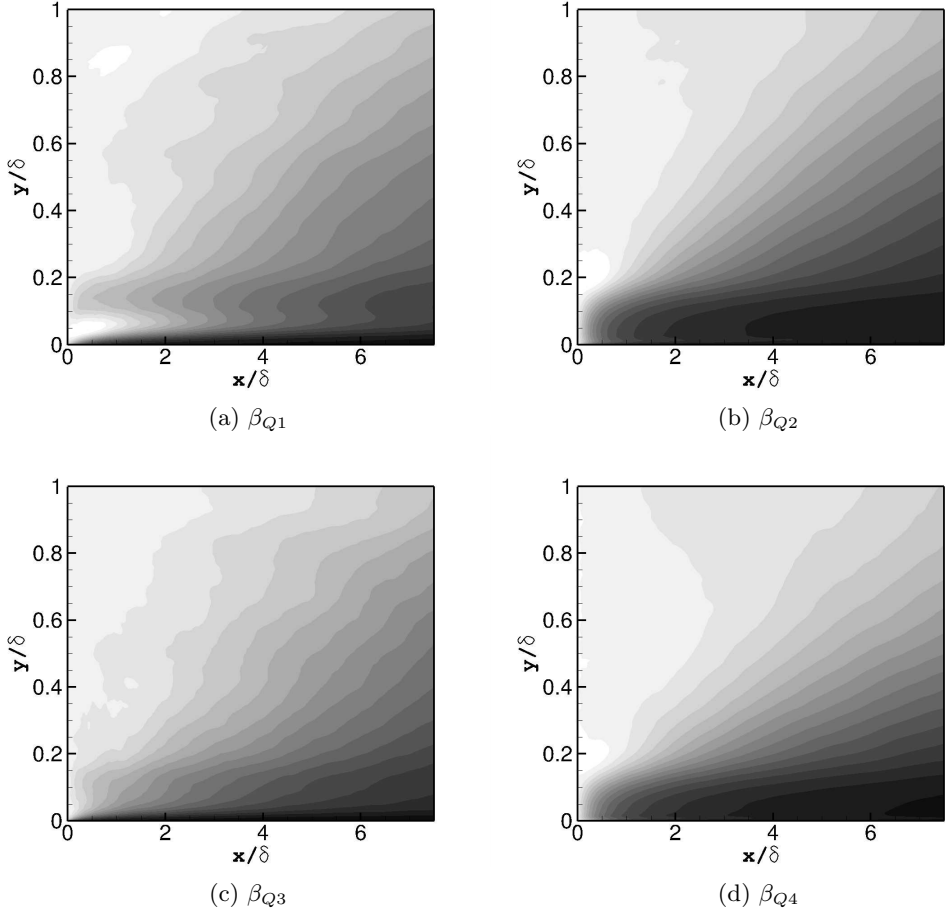


Figure 19: Normalized recovery magnitudes for different components of the quadrant analysis of  $\overline{u'v'}$  for case B. Scale: black 0.0, white 1.0.

close to the wall, and in the outer-flow. This behaviour is more apparent from the local Kolmogorov lengthscale,  $\eta = (\nu^3/\epsilon)^{0.25}$ , in figure 20d.

$P$  too, as a general rule, shows higher levels caused by the underlying roughness, except within the roughness cavity, where destruction of the smooth-wall buffer layer inhibits near-wall turbulence generation. On the developing smooth wall, however, by the second streamwise profile the roughness peak of  $P$  has virtually vanished, and has been replaced by the near-wall smooth-wall peak. The roughness induced small scales, upon removal of their source, disappear rapidly, resulting in a sharp initial reduction of  $\epsilon$ . Despite this, at the last streamwise station, it is still about 50% higher than its fully developed counterpart.

The behaviour of  $P/\epsilon$  in figure 20b is primarily determined by  $\epsilon$ . The continuing stronger  $\epsilon$ , along with more complete and quick recovery of  $P$ , results in  $P/\epsilon$  showing a minimum, not different from that observed in fully developed smooth walls, but displaced upwards due to the top-wall bias of the mean velocity. Closer to the lower wall, in the region where  $P/\epsilon$  is near unity for fully developed smooth walls, and again due to much a stronger dissipation rate,  $P/\epsilon$  is suppressed to about 0.5 – 0.6. The momentary increase

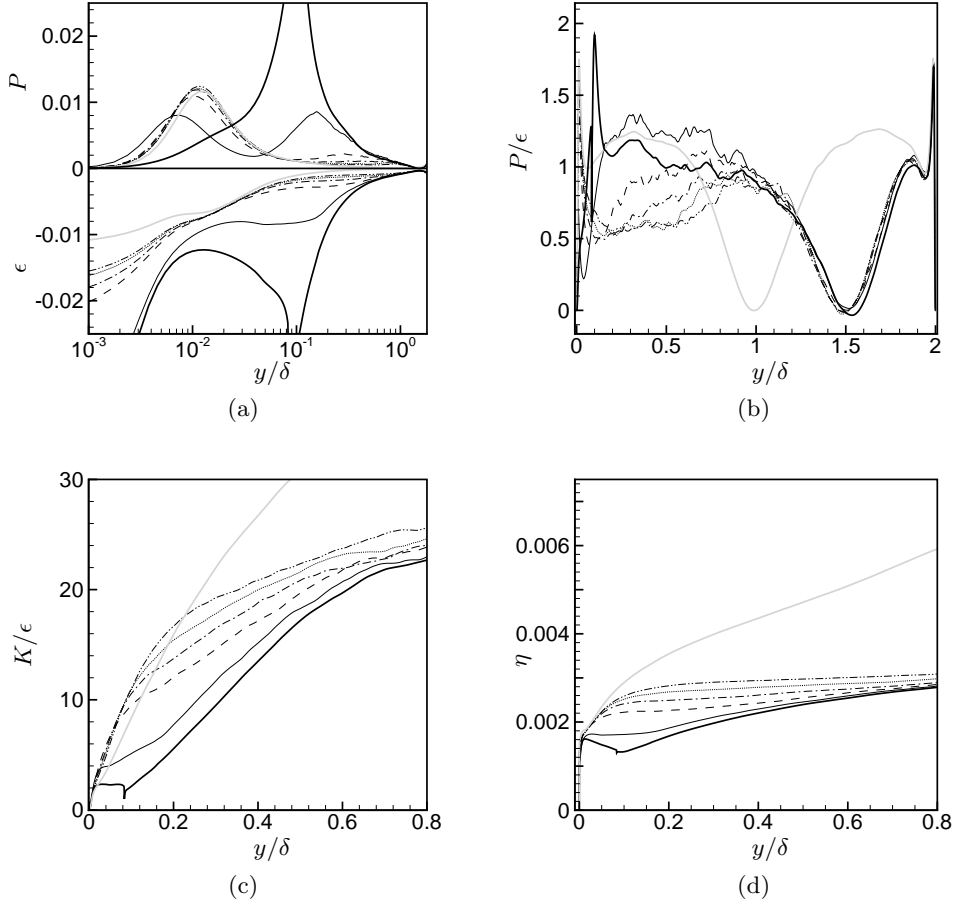
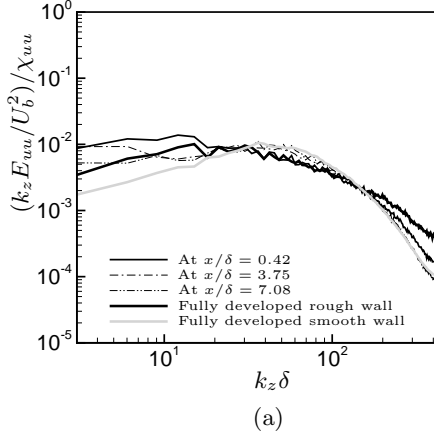


Figure 20: Wall normal variation of (a)  $P$  and  $\epsilon$  terms in the TKE budget equation, (b)  $P/\epsilon$ , (c) turbulence time-scale  $K/\epsilon$  and (d) the Kolmogorov length-scale  $\eta = (\nu^3/\epsilon)^{0.25}$  for case B. — in the fully developed rough-wall regime, — at  $x/\delta = 0.42$ , — at  $x/\delta = 2.08$ , - - - at  $x/\delta = 3.75$ , ····· at  $x/\delta = 5.42$ , - - - at  $x/\delta = 7.08$ , — from fully developed smooth-wall channel flow. Normalization of vertical axes is using the outer variables:  $U_b$  and  $\delta$ .

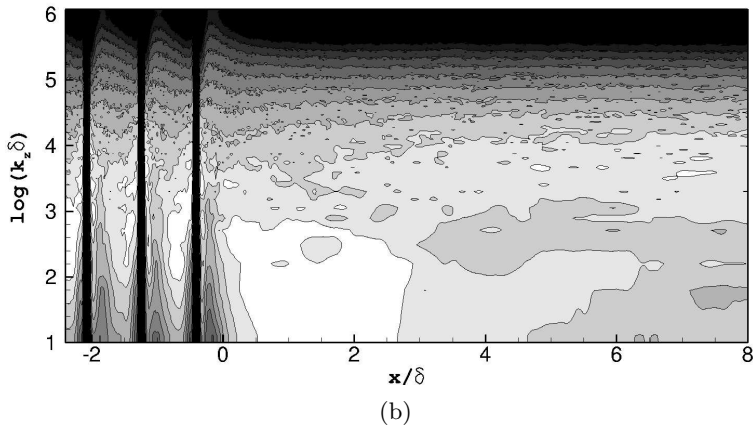
at the first streamwise station is a consequence of strong streamwise inhomogeneity in  $P/\epsilon$  just above the roughness.

Because of higher  $\epsilon$ , the turbulence time-scale  $K/\epsilon$  in figure 20c is also diminished below the fully developed smooth-wall value. With downstream distance, the turbulence time-scale shows a slow increase towards the higher, fully developed levels. This can only be due to a faster recovery of  $\epsilon$  towards equilibrium values, in relation to  $K$ , which is predominantly composed of slow recovering large-scales.

The near-wall energy spectra of turbulence fluctuations allow the recovery at small and at large scales of turbulence to be distinguished. The near-wall behaviour of pre-multiplied, energy spectra,  $k_z E_{\alpha\alpha}(x, y)$ , as a function of spanwise wavenumber,  $k_z$ , is shown in figure 21. For fully developed smooth-wall flow, the wall-normal location in this figure corresponds to  $y^+ \approx 20$ . To account for downstream decay of turbulence, at each



(a)



(b)

Figure 21: Normalized, pre-multiplied spanwise energy spectra at  $y/\delta = 0.023$  for case B. (a)  $(k_z E_{uu}/U_b^2)/\chi_{uu}$  at discrete streamwise stations. The fully developed rough-wall profile is located at  $x/\delta = 0$ . (b)  $(k_z E_{uu}/U_b^2)/\chi_{uu}$  in the continuous domain. Scale: white  $10^{-2}$ , black  $5(10^{-4})$ . The vertical lines for  $x < 0$  in (b) indicate the location of the roughness elements.

streamwise station  $k_z E_{\alpha\alpha}/U_b^2$  is normalized by

$$\chi_{\alpha\alpha} = \int_0^{2\pi N_k/L_z} \frac{k_z E_{\alpha\alpha}}{U_b^2} d(k_z \delta).$$

Here,  $N_k$  is the total number of wavenumbers in the spanwise direction. On entering the transitional regime, the energy in the small scales shows the expected immediate drop, while at large scales there is an injection of energy. This is more clear from the white patch in the contour plot in figure 21b. The initial increment of energy is attributed to downward reversion of the upward shifted turbulence structure over the rough-wall. The intermediate scales exhibit slow downstream evolution, which in turn implies slow readjustment of the turbulence cascade near the developing smooth wall.

To compare the spectral recovery among different cases, profiles at fixed streamwise stations ( $x/\delta$ ) are plotted in figure 22. For intermediate and large wavenumbers ( $k_z \delta >$

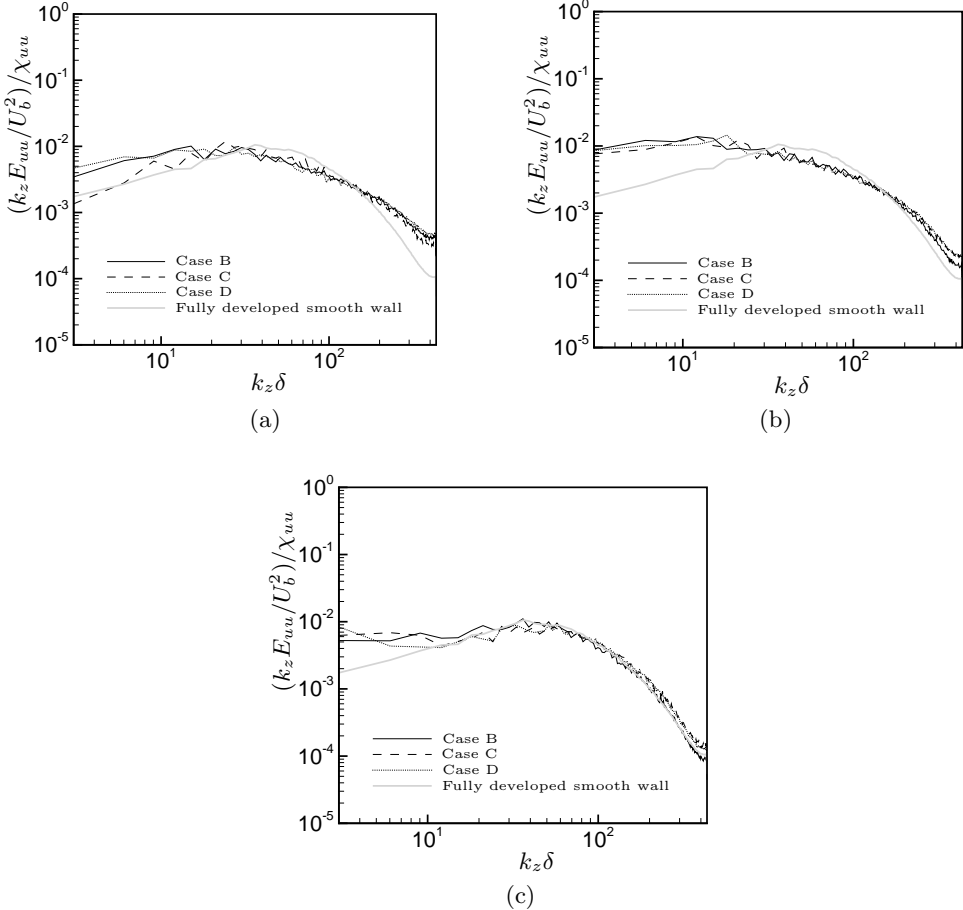


Figure 22: Normalized, pre-multiplied spanwise energy spectra,  $(k_z E_{uu}/U_b^2)/\chi_{uu}$ , at  $y/\delta = 0.023$  at (a)  $x/\delta = 0$ , (b)  $x/\delta = 0.42$  and (c)  $x/\delta = 7.08$ .

30), a reasonable collapse is observed. The recovery at these intermediate and small scales thus progresses very similarly for all roughness cases considered here. Nonetheless, further studies with different roughnesses are needed to shed more light on the matter.

Figure 23 shows the energy spectra,  $E_{uu}/U_b^2$ , as a function of the spanwise wavenumber at different streamwise location and two wall-normal heights. The  $k_z^{-5/3}$  scaling is clearly established, both near the wall, at  $y/\delta = 0.1$  in figure 23a, and at the channel center-line in figure 23b. There is a sharp reduction in energy at large wavenumbers, but clearly not as severe as seen in figure 21, at  $y/\delta = 0.023$ . The channel center-line shows negligible spectral recovery at large wavenumbers, which agrees with the results of  $\epsilon$  from figure 20. The wall-normal dependence of energy spectra is plotted in figure 24 for two streamwise locations. Little change occurs with downstream distance near the upper smooth wall. However, close to the lower wall, at about  $y/\delta < 0.4$ , significant reduction in energy is observed. This reduction is broadband and a direct result of the removal of roughness. The decrease in energy is particularly intense at small wavenumbers; these small wavenumbers also show an increase in the spanwise lengthscale. At large wavenumbers and near the

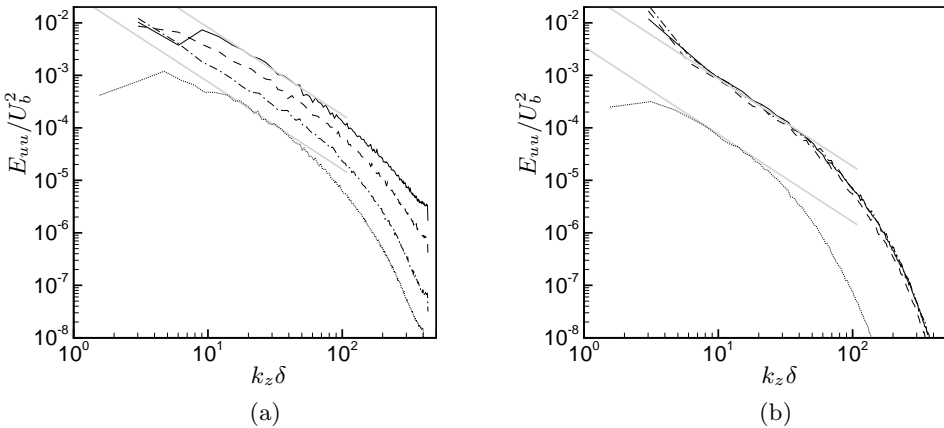


Figure 23: Energy spectra,  $E_{uu}/U_b^2$ , as a function of spanwise wavenumber for case B (a) at  $y/\delta = 0.1$  and (b) at  $y/\delta = 1.0$ . — at  $x/\delta = -1.67$ , - - - at  $x/\delta = 0.42$ , - · - - at  $x/\delta = 3.75$ , and ····· from smooth-wall channel flow. —  $E_{uu}/U_b^2 = A(k_z \delta)^{-5/3}$ .

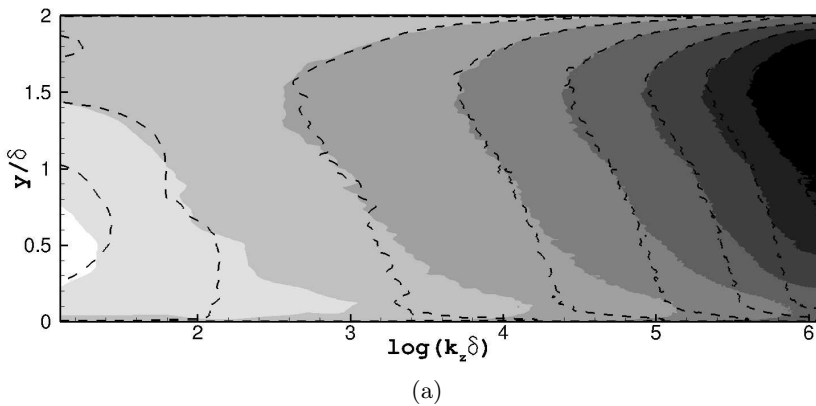


Figure 24: Wall-normal distribution of spanwise energy spectra,  $E_{uu}/U_b^2$ , for case B. Grayscale contours: at  $x/\delta = -1.67$ , and dashed lines: at  $x/\delta = 3.75$ . Scale: white 0.02, black  $10^{-8}$ .

channel center, the asymmetry in the wall-normal distribution of energy persists. This trend is consistent with the downstream relaxation of  $\epsilon$  in figures 20a and 20b.

The spectra highlight that very close to the wall, at  $y^+ = 20$ , the rough-wall induced fine-scale motion quickly disappear once the roughness is removed. At large-scales, however, there is an initial increase in the energy due to the turbulence which was displaced upward by the roughness, and which shifts downwards on transitioning to the smooth section. The expected streamwise decay follows, after this initial increase. Like the results of other turbulence quantities presented earlier, e.g.  $\overline{u'_i u'_j}$  and  $\epsilon$ , the recovery over the entire wavenumber range progresses quickly near the wall relative to a slow recovery in the outer flow.

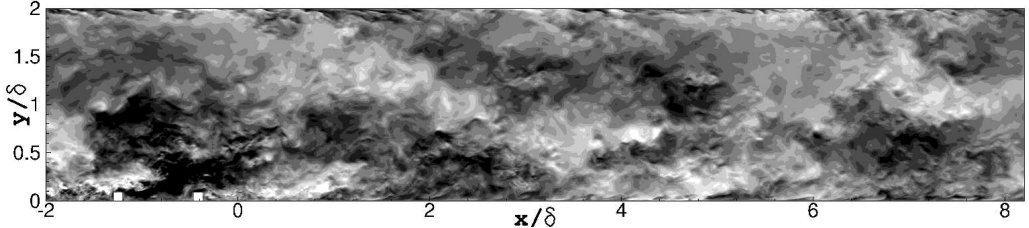


Figure 25: Instantaneous streamwise velocity fluctuations  $u'$  in the  $xy$ -plane for case B. Scale: white +0.3, black -0.3.

#### *Instantaneous visualizations*

Figure 25 is a side-view of the instantaneous streamwise velocity fluctuations, for a portion of the RTS regime. A fully developed smooth-wall is characterized by intermittent, low-intensity eddies, that diffuse into the outer flow. This is in contrast to a rib-roughened wall, which is highly active and shows large-scale structures, of several rib-spacings in length, above the roughness, along with much stronger, three-dimensional eddies, being created by the roughness elements (figures 1). Instantaneously, the size of these large-scale structures can vary between 3 and less than one rib-spacings. Such large structures are seen in figure 25 for  $x/\delta \lesssim 1$ ,  $y/\delta \lesssim 1$ . Figure 1 also shows these large structures above the roughness in the form of three separate white patches with streamwise size of approximately 2 rib-spacings. The origin of these structures is uncertain; they seem to emerge from an interaction between the underlying roughness and the flow above it. Preliminary visualizations from RTS simulations using cube-roughened walls (not presented here) also support the presence of large-scale structures above the roughness, albeit of comparatively smaller size and weaker intensity. The turbulence statistics for these cube-roughened walls, however, including the mean velocity and turbulence stresses, are qualitatively quite similar to the results presented here.

The impact of the upstream rough wall on qualitative recovery of the near-wall large-scale turbulence structure is more apparent from the  $xz$ -plane visualizations of instantaneous  $u'$  in figure 26. The wall-normal height for these  $xz$ -planes lies within the buffer-layer and corresponds to  $y^+ \approx 20$  in fully developed smooth-wall flows. At this wall-normal height, the rough-wall zone contains high-intensity fluctuations, of small length and time-scales. After RTS transition, however, there is an immediate reversion towards much larger length-scales that are evident as early as  $x/\delta \approx 0.5$  in figure 26. Much stronger and larger turbulence structures, continue to hinder the near-wall structural recovery and intermittently perturb the familiar high-speed and low-speed streaks, which are characteristic of fully developed smooth walls (Durbin & Reif 2011). As mentioned earlier, these large-scale structures are an injection turbulence that had shifted upwards over the rough-wall, and now reverts downwards. Figure 27 shows an instantaneous  $u'$  snapshot in the  $xz$ -plane just above the roughness elements, at  $y/\delta = 0.108$ . This wall-normal location is characterized by large structures with spanwise size of the order of about one rib-spacing, that show slight thickening after the RTS transition. This is indicated by the large white patch forming at  $x/\delta \approx 3$  and  $z/\delta \approx 1$  in figure 27. The spanwise enlargement of turbulence structure is coupled with the expected reduction in turbulence intensity, which is reflected by the contours becoming less distinct.

Further evidence for presence of these wider turbulence structures in the developing regime, is provided by the integral of spanwise two-point correlations,  $R_{\alpha\alpha}^z$ , in figure 3. Compared to the rough wall, the developing smooth wall at  $x/\delta = 5$  in figure 3

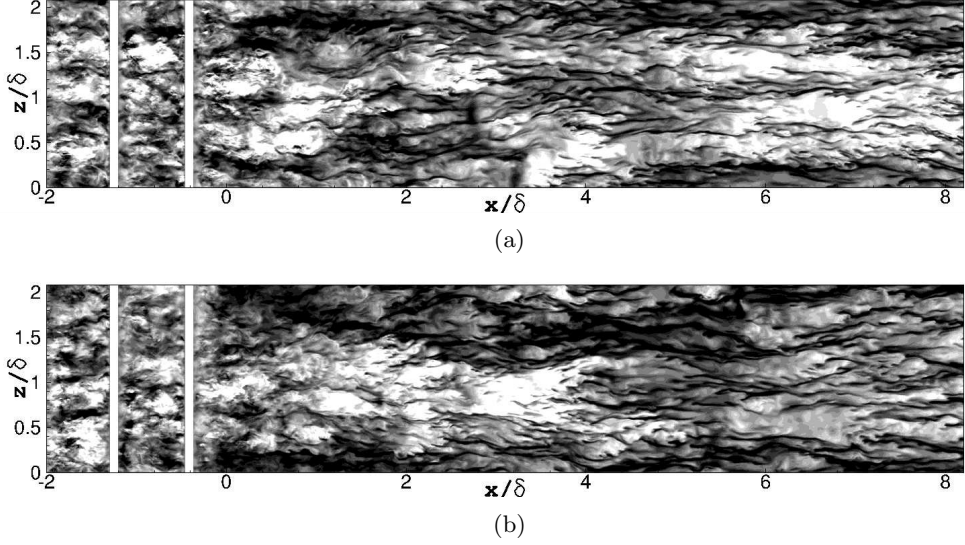


Figure 26: Instantaneous streamwise velocity fluctuations  $u'$  in the  $xz$ -plane for case B at  $y/\delta = 0.023$ . (a) at  $tU_b/\delta = t_1$ , and (b) at  $tU_b/\delta = t_1 + 8.2$ . Scale: white +0.2, black -0.2. The vertical lines for  $x < 0$  indicate the location of the roughness elements.

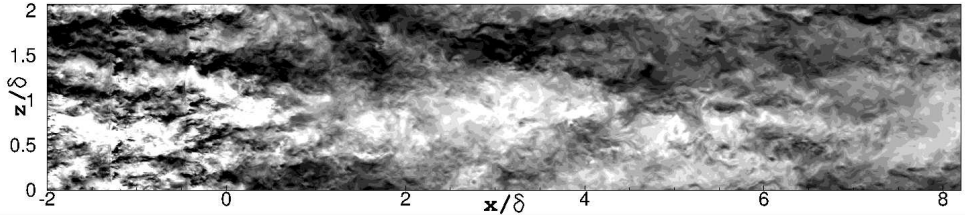


Figure 27: Instantaneous streamwise velocity fluctuations  $u'$  in the  $xz$ -plane for case B at  $y/\delta = 0.108$ . This wall-normal location corresponds to  $y^+ \approx 100$  in a fully developed smooth-wall channel flow. Scale: white +0.3, black -0.3.

shows a significant increase in the spanwise integral length-scale, for all three fluctuating velocities.

As also shown in figure 28, immediately after the RTS transition, there is a sharp increase in the streamwise integral length-scale of  $u'$  fluctuations,  $L_{uu}$ , for  $y/\delta \lesssim 0.2$ . The streamwise integral length-scale,  $L_{uu}$ , for our RTS simulations is calculated by identifying the first minimum in the correlation curve for  $R_{uu}^x$  and then calculating the integral up to this minimum. The near-wall streamwise structures immediately after the step change in roughness, that are influenced by large-scales above the rough wall, are larger than their fully developed counterparts. As mentioned previously, these rough-wall large-scales have a streamwise extent of about  $1.5\delta$  (or approximately two rib-spacings).

After the RTS transition, near the wall the reversion to much stronger mean shear (see figures 4b and 9) results in quick re-emergence of the characteristic smooth-wall streaky structure. However, this strong mean shear near the wall does not prevent the large rough-wall structures from sporadically influencing the elongated streaks. Furthermore, further out, the weaker mean shear fails to effectively break up the large structures, which

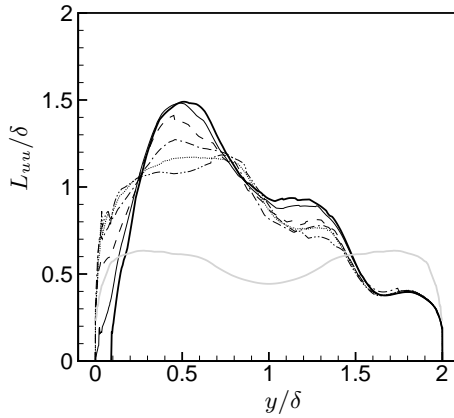


Figure 28: Variation of the streamwise integral length-scale,  $L_{uu}$ , in the vicinity of step change in roughness for case B in the wall-normal direction. — at  $x/\delta = -0.55$ , — at  $x/\delta = -0.21$ , - - - at  $x/\delta = 0.49$ , - · - · - at  $x/\delta = 1.18$ , · · · · at  $x/\delta = 1.88$ , - - - - at  $x/\delta = 2.57$ , — from fully developed smooth-wall channel flow.

results in them continuing downstream. This, in addition to figure 28, can also be seen from figure 25 in the form of black patches continuing in the developing regime at about  $y/\delta \approx 0.8$ .

#### 4. Summary and conclusions

The development of a fully developed, rib-roughened turbulent channel flow, proceeding over a smooth wall, has been studied by direct numerical simulations. These numerical experiments are the first of this configuration. Both statically averaged data and instantaneous visualizations have been discussed. The parameter  $\delta/k$  is kept larger than most previous fully developed rough-wall simulations. All four test cases fall in the fully-rough regime,  $r^+ > 90$ .

The initial, fully developed regime generates realistic turbulent inflow conditions for the subsequent transitional regime, and is long enough to effectively break up the large structures. A long rough wall region is necessary to minimize the contamination of large scale statistics like  $u'u'$  over the developing smooth wall.

After the RTS transition, the skin friction,  $C_f$ , shows a sharp reduction before recovering quickly and virtually levelling off by  $x \approx 2\delta$ . Even so, reversion to fully developed magnitudes fails to occur. The mean velocity and Reynolds stresses profiles show a slow recovery; by the last streamwise station, at  $x/\delta = 7.08$ , considerable mismatch with the symmetric, smooth-wall channel flow profiles remains. Extrapolations are provided that recovery might occur after  $x \approx 40$  to  $55\delta$ . Since the effect of step change in roughness is spread across the whole wall-normal extent of the channel, the traditional concept of an internal boundary layer height does not apply. An equilibrium log layer, also, does not develop within the domain. From mean-velocity and skin-friction viewpoints, the transitional regime could be divided roughly into two zones: an initial strong non-equilibrium zone within  $0 < x/\delta < 0.5$ , followed by a weak non-equilibrium zone from  $x/\delta > 0.5$ . In the near-wall region of the strong non-equilibrium zone (see figure 11b),  $\overline{U}^+$  increases with downstream distance, while the opposite trend is observed farther

from the wall. This is a consequence of strong variation in  $C_f$  immediately after the RTS transition.

By the end of the computational domain, turbulence stresses still show a strong mismatch with smooth-wall channel flow results, except in a thin layer very close to the wall. Above the thin wall layer, much higher turbulence persists throughout. It is carried downstream from the upstream, rough wall. From normalized recovery magnitudes and quadrant analysis, it is evident that the shear-stress producing motions recover more quickly than large structures associated with  $\overline{u'u'}$  above the thin, wall layer. Gradients of momentum fluxes, that are influenced by the roughness size, contribute significantly to the overall momentum balance, and this balance is not just between pressure gradient and shear-stress — as in fully developed regimes.

The rough wall creates a high dissipation rate,  $\epsilon$ . In the transitional regime, upon removal of the roughness elements,  $\epsilon$  decays rapidly. But by the end of the computational domain,  $\epsilon$  is still about 50% higher than the equilibrium smooth wall level. The higher  $\epsilon$  results in a smaller turbulence time-scale,  $K/\epsilon$ , persisting over the smooth wall.

Instantaneous visualizations of  $u'$  contours display the presence of large structures, of several ribs-spacings in size, above the rough wall. These large structures continue downstream into the transitional regime, except for reverting downwards. They influence the near-wall structural recovery. Evidence for these large structures is also provided by the spanwise energy spectra in figure 21 and by the streamwise integral length-scale in figure 28. Elongated streaks, appear promptly after the RTS transition, but they are being intermittently perturbed by the ambient large structures.

This work was supported by the Office of Naval Research under award #N00014-17-1-2200 and by the US Army under contract #W911W6-14-C-0003.

## REFERENCES

- ANDREOPoulos, J & WOOD, DH 1982 The response of a turbulent boundary layer to a short length of surface roughness. *Journal of Fluid Mechanics* **118**, 143–164.
- ANTONIA, RA & LUXTON, RE 1971 The response of a turbulent boundary layer to a step change in surface roughness part 1. smooth to rough. *Journal of Fluid Mechanics* **48** (4), 721–761.
- ANTONIA, R. A. & LUXTON, R. E. 1972 The response of a turbulent boundary layer to a step change in surface roughness. part 2. rough-to-smooth. *Journal of Fluid Mechanics* **53**, 737–757.
- ASHRAFIAN, ALIREZA, ANDERSSON, HELGE I. & MANHART, MICHAEL 2004 DNS of turbulent flow in a rod-roughened channel. *International Journal of Heat and Fluid Flow* **25** (3), 373 – 383, turbulence and Shear Flow Phenomena (TSFP-3).
- CHENG, H. & CASTRO, IAN P. 2002 Near-wall flow development after a step change in surface roughness. *Boundary-Layer Meteorology* **105** (3), 411–432.
- DURBIN, PAUL A. & REIF, B. A. PETTERSSON 2011 *Statistical Theory and Modeling for Turbulent Flows*. Wiley.
- HANJALIC, K. & LAUNDER, B. E. 1972 Fully developed asymmetric flow in a plane channel. *Journal of Fluid Mechanics* **51**, 301–335.
- HANSON, R. E. & GANAPATHISUBRAMANI, B. 2016 Development of turbulent boundary layers past a step change in wall roughness. *Journal of Fluid Mechanics* **795**, 494–523.
- HILL, ARCHIBALD VIVIAN 1913 The combinations of haemoglobin with oxygen and with carbon monoxide. i. *Biochemical Journal* **7** (5), 471.
- HOSNI, MH & COLEMAN, HW 1993 Relaxation of the turbulent boundary layer after an abrupt change from rough to smooth wall. *Journal of fluids engineering* **115**, 379.
- IKEDA, T. & DURBIN, P. A. 2002 Direct simulations of a rough-wall channel flow. Report no.

- TF-81, Stanford University, Flow Physics and Computation Division, Dept. of Mechanical Engineering.
- IKEDA, TOMOAKI & DURBIN, PAUL A. 2007 Direct simulations of a rough-wall channel flow. *Journal of Fluid Mechanics* **571**, 235–263.
- JACOBI, I. & MCKEON, B. J. 2011 New perspectives on the impulsive roughness-perturbation of a turbulent boundary layer. *Journal of Fluid Mechanics* **677**, 179–203.
- JIMNEZ, JAVIER 2004 Turbulent flows over rough walls. *Annual Review of Fluid Mechanics* **36** (1), 173–196, arXiv: <http://dx.doi.org/10.1146/annurev.fluid.36.050802.122103>.
- KIM, HOT, KLINE, SJ & REYNOLDS, WC 1971 The production of turbulence near a smooth wall in a turbulent boundary layer. *Journal of Fluid Mechanics* **50** (1), 133–160.
- LEONARDI, STEFANO & CASTRO, IAN P. 2010 Channel flow over large cube roughness: a direct numerical simulation study. *Journal of Fluid Mechanics* **651**, 519539.
- LEONARDI, S, ORLANDI, PAOLO, SMALLEY, RJ, DJENIDI, L & ANTONIA, RA 2003 Direct numerical simulations of turbulent channel flow with transverse square bars on one wall. *Journal of Fluid Mechanics* **491**, 229–238.
- MARUSIC, IVAN, MONTY, JASON P, HULTMARK, MARCUS & SMITS, ALEXANDER J 2013 On the logarithmic region in wall turbulence. *Journal of Fluid Mechanics* **716**.
- MEHDI, FARAZ, KLEWICKI, JC & WHITE, CM 2013 Mean force structure and its scaling in rough-wall turbulent boundary layers. *Journal of Fluid Mechanics* **731**, 682–712.
- MIYAKE, Y., TSUJIMOTO, K. & NAGAI, N. 2002 Numerical simulation of channel flow with a rib-roughened wall. *Journal of Turbulence* **3**, 035.
- MOSER, ROBERT D., KIM, JOHN & MANSOUR, NAGI N. 1999 Direct numerical simulation of turbulent channel flow up to  $Re_\tau = 590$ . *Physics of Fluids* **11** (4), 943–945.
- NAGANO, YASUTAKA, HATTORI, HIROFUMI & HOURA, TOMOYA 2004 DNS of velocity and thermal fields in turbulent channel flow with transverse-rib roughness. *International Journal of Heat and Fluid Flow* **25** (3), 393 – 403, turbulence and Shear Flow Phenomena (TSFP-3).
- NIKURADSE, J. 1933 Strömungsgesetze in Rauben Rohren. *Verein Deutsher Ingenieure, Forschungsheft* p. 361.
- ORLANDI, PAOLO, LEONARDI, S & ANTONIA, RA 2006 Turbulent channel flow with either transverse or longitudinal roughness elements on one wall. *Journal of Fluid Mechanics* **561**, 279–305.
- PEARSON, BR, ELAVARASAN, R & ANTONIA, RA 1997 Effect of a short roughness strip on a turbulent boundary layer. *Applied scientific research* **59** (1), 61–75.
- PERRY, ANTHONY EDWARD, SCHOFIELD, WILLIAM H & JOUBERT, PETER N 1969 Rough wall turbulent boundary layers. *Journal of Fluid Mechanics* **37** (02), 383–413.
- PIERCE, C. D. & MOIN, P. 2004 Progress-variable approach for large-eddy simulation of non-premixed turbulent combustion. *Journal of Fluid Mechanics* **504**, 73–97.
- RAUPACH, MR, ANTONIA, RA & RAJAGOPALAN, S 1991 Rough-wall turbulent boundary layers. *Appl. Mech. Rev* **44** (1), 1–25.
- SQUIRE, DT, MORRILL-WINTER, C, HUTCHINS, N, SCHULTZ, MP, KLEWICKI, JC & MARUSIC, I 2016 Comparison of turbulent boundary layers over smooth and rough surfaces up to high reynolds numbers. *Journal of Fluid Mechanics* **795**, 210–240.
- VOLINO, RALPH J, SCHULTZ, MICHAEL P & FLACK, KAREN A 2011 Turbulence structure in boundary layers over periodic two-and three-dimensional roughness. *Journal of Fluid Mechanics* **676**, 172–190.
- WALLACE, JAMES M 2016 Quadrant analysis in turbulence research: history and evolution. *Annual Review of Fluid Mechanics* **48**, 131–158.
- WALLACE, JAMES M, ECKELMANN, HELMUT & BRODKEY, ROBERT S 1972 The wall region in turbulent shear flow. *Journal of Fluid Mechanics* **54** (1), 39–48.
- WEI, T, FIFE, P, KLEWICKI, J & McMURTRY, P 2005 Properties of the mean momentum balance in turbulent boundary layer, pipe and channel flows. *Journal of Fluid Mechanics* **522**, 303–327.